Differential Sputtering Yields of Refractory Metals by Xenon, Krypton, and Argon Ion Bombardment at Normal and Oblique Incidences

IEPC-2005-293

Presented at the 29th International Electric Propulsion Conference, Princeton University, October 31 – November 4, 2005

Kirk A. Zoerb*, John D. Williams†, Desiree D. Williams‡, and Azer P. Yalin§
Colorado State University, Fort Collins, CO, 80523, USA

Abstract: Differential sputter yields are reported for Molybdenum, Tantalum, and Tungsten after exposure to Xenon, Krypton, and Argon ion bombardment at multiple angles of incidence (0 - 60°) and ion energies (150 - 1500 eV). Differential yields were measured by sweeping a Quartz Crystal Microbalance (QCM) in a semi-circular arc over a given target in the plane defined by the target normal and ion beam axis. Differential yields were integrated to obtain total sputter yields. The measured total yields were generally less than, but comparable to, published values. The dependence of total yield on angle of incidence was also investigated. The total yields were found to be largest for angles of incidence between 45° and 60°. The effects of the bombarding ion energy and the ion mass-to-target atom mass ratio on the differential yield distributions are discussed. In addition, preliminary measurements of differential sputter yields as a function of both polar and azimuthal angles are presented.

Nomenclature

A_s	=	QCM sensor area (cm^2)
J	=	current (mA)
j	=	current density (mA/cm^2)
J_+	=	singly ionized particle current (mA)
J_{++}	=	doubly ionized particle current (mA)
J_b	=	beam current (mA)
j_b	=	beam current density (mA/cm^2)
M_t	=	target molecular mass (amu)
q	=	electronic charge unit (1.6×10^{-19} Coulombs)
$R(\alpha)$	=	mass accumulation rate (gm/s)
R_{arm}	=	radial position of Faraday probe measured from the motor's axis of rotation (cm)
R_{beam}	=	radial position from the ion beam's central axis (cm)
r_{qcm}	=	distance of QCM from target center (cm)
V_a	=	accelerator (accel) grid potential (V)
V_D	=	discharge voltage (V)

* Graduate Research Assistant, Mechanical Engineering Department, kaptkz@engr.colostate.edu.
† Assistant Professor, Mechanical Engineering Department, johnw@engr.colostate.edu.
‡ Graduate Research Assistant, Mechanical Engineering Department, daisyw@engr.colostate.edu.
§ Assistant Professor, Mechanical Engineering Department, ayalin@engr.colostate.edu

V_s = screen grid potential (V)
y = differential sputtering yield (atoms/ion/steradian)
Y = total sputtering yield (atoms/ion)
Z = atomic number
α = QCM sensor angle from target normal (°)
β = ion incidence angle from target normal (°)
θ_{arm} = angular position of the Faraday cup (°)
ϕ = azimuthal angle in the target plane from the plane containing the ion beam and target normal (°)

I. Introduction

Sputter erosion of surfaces is of great importance for electric propulsion (EP) thrusters and spacecraft employing such thrusters. Sputtering has been identified as a major concern in 80% of the possible failure modes of an electrostatic thruster[1], and sputtering of spacecraft surfaces has resulted in property modification of surface materials. Additionally, deposition of sputtered products onto other spacecraft surfaces can result in modification of surface material properties, or contamination. In order to model the effects of sputter erosion it is critical to have detailed fundamental sputter erosion data. Typically, the data used for modeling of EP lifetime (sputter erosion) and/or erosion of spacecraft surface materials is expressed in terms of the total sputter yield, *Y*, (i.e. the number of sputtered atoms per incident ion) and provides no information regarding the spatial distribution of the sputtered particles. A cosine (diffuse) distribution of sputtered particles is often assumed[2,3] regardless of the angle of incidence of the sputtering atoms or molecules. However, angularly resolved (differential sputter yield) measurements[4-10] have shown that the assumption of a cosine distribution is inappropriate for low energy incident ions, especially for non-normal angles of incidence.

Differential yield distributions are useful, for example, in determining thruster locations where sputtered material can deposit. Such deposits can lead to build-up and flaking and may cause electrical or contamination problems[7]. Thus, the differential yield data are of paramount importance when determining where equipment sensitive to surface contamination (e.g. optical devices and photovoltaics) can be located. Also, when designing vacuum chamber beam dumps the differential yield data could be used to determine the optimum orientation of surfaces that minimizes deposition of back-sputtered beam dump material onto EP test devices, thereby considerably improving the quality of wear test measurements. Accordingly, differential yield data can be used to significantly increase the accuracy of ion optics wear models.

Certain computer models, such as TRIM, calculate differential yields but tend not to be accurate at the low ion energies of interest[11]. Therefore, it is important to have accurate experimental distributions that can be compared to (future) improved models developed for low ion energy. A successful example of this synergy is the good agreement between a molecular dynamics simulation code[12] and measured differential yields by Doughty[13] for Ar^+ on Cu.

Recent studies[6-9] into the differential yield of materials (of interest to the EP community) use spectrometry methods such as Rutherford Backscattering (RBS) and Quadra-pole Mass Spectrometry (QMS) and provide total yield measurements in agreement with other published data. These studies have generally been at normal incidence for low energies and have found under-cosine shaped distributions, similar to those found in other studies[4-10]. Many other noteworthy studies[14-18] have been conducted using differing techniques to obtain angular distributions. Quartz Crystal Microbalance (QCM) based studies by Williams[4,5] have shown angular distributions for oblique incident ions bombarding carbon materials at multiple energies and have total yields in reasonable agreement with other published data. Angular distributions have also been measured using laser induced fluorescence measurement techniques for EP[19] and non-EP[20] related materials and other work at Colorado State University has recently demonstrated the use of cavity ring-down spectroscopy (CRDS) for high-sensitivity detection of sputtered particles[21,22]. Recently, Kolasinksi[23] (using a QCM method) and Tartz[24] (using a weight loss technique) investigated total yields as a function of angle of incidence. Also of note is Stepanova[25,26] who has performed computer modeling of surface texture effects on sputtering at non-normal incidence.

This paper is organized by first describing the experimental apparatus and test procedures in Section II. This section also contains a discussion of the ion beam distribution over the target, data analysis procedures, and a description of how full azimuthal and polar angle measurements were performed. Section III contains a discussion of normal incidence tests followed by oblique incidence tests. This section includes a comparison to results that are available in the literature, and a detailed analysis of the major assumptions that are made to reduce the measurements.

II. Experimental Set-up

This section discusses the vacuum chamber, ion source, and ion optics used to sputter the target materials. It also provides details on the QCM, experimental procedure, data acquisition and data analysis.

A. Vacuum Chamber/Ion Source

A 0.125 m^3 stainless steel vacuum chamber (43 cm ID x 76 cm long main section), equipped with a 1500 liter/s CTI-8 cryogenic pump, was used for all of the experiments described herein. With a base pressure of 5×10^{-7} Torr (after 8-hour bake out), it maintained working pressures of between 5×10^{-5} Torr to 9×10^{-5} Torr. The main background gas contaminate measured by a Ferran MPA residual gas analyzer (RGA) was N_2 (or CO) at a pressure of 2 x 10^{-7} Torr followed by H_2O at 1.2×10^{-7} Torr.

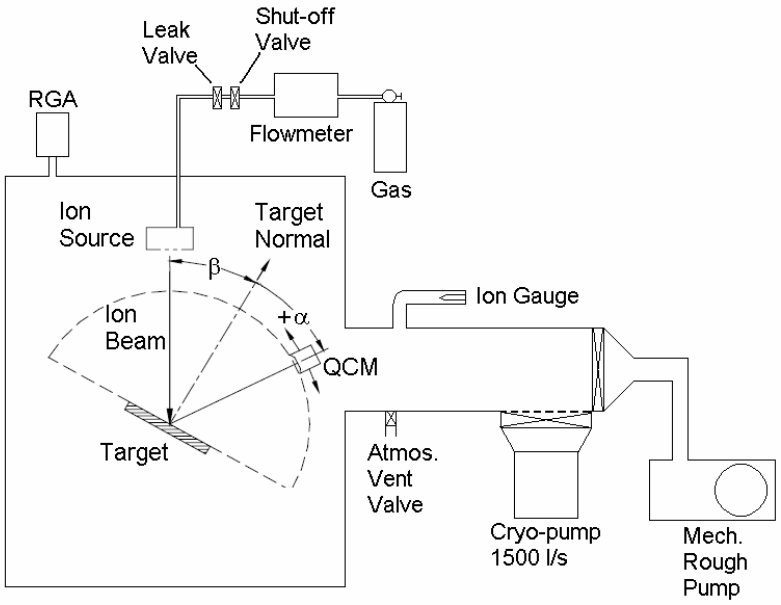

Figure 1. Vacuum system and ion source set-up.

The ion source was comprised of a discharge chamber, into which neutral gas flowed at a set flow rate. The neutral gas was ionized using a tungsten hot-filament cathode, and the ion optics used to extract and focus the ion beam consisted of a two-grid Poco graphite system. A tungsten hot-filament neutralizer was located 1 cm downstream of the accelerator grid. The neutralizer emission current was set at 150% of the beam current to negate the space charge effect and neutralize the extracted ion beam. The discharge voltage (V_D) was set between 30 V and 35 V to minimize the number of multiply charged ions produced. Three different gases were used by the ion source in the process of this investigation: xenon, krypton, and argon.

A rotatable, water-cooled target was placed 23 cm downstream of the ion source. Target materials investigated were molybdenum, tantalum, and tungsten; all of which were at least 99.9% pure. The ion beam extracted from the ion source was directed toward the target as indicated in Fig. 1. For each configuration, a QCM was used to obtain the differential sputter yield distribution by sweeping it over the target (about the axis of target rotation) so as to ensure the viewing of the same point on the target throughout the sweep. The QCM was placed, via an extended arm, 17.4 cm (r_{qcm}) from target center. The polar angle of the QCM from the target normal is defined as α, whereas the angle of the ion beam from the target normal is defined as β (the angle of incidence). We refer to sputtered particles with $\alpha > 0$ as forward-sputtered and, conversely, $\alpha < 0$ as back-sputtered.

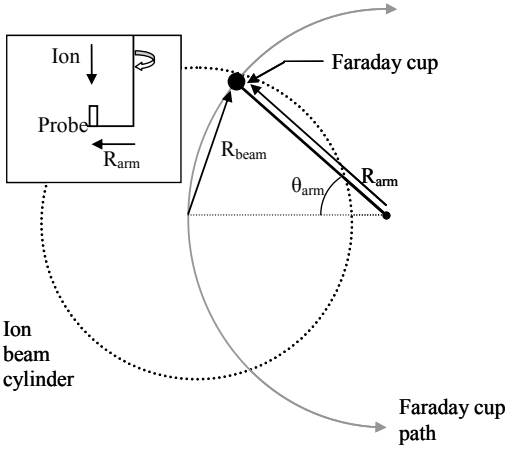

Figure 2. Diagram of the Faraday cup path through the ion beam.

B. Beam Characterization

Two assumptions are made with the QCM method: 1) the beam spot size on the target is small and 2) the ions arrive at the same angle of incidence, β. These assumptions provided a straightforward way to calculate the differential

yield at a given value of β. A screened Faraday probe was used to measure the current density variation of the ion beam at the target to investigate the validity of this beam spot assumption in our set-up.

For each beam energy investigated, a set of Faraday probe measurements were taken in the $\beta = 0°$ target plane in order to identify the operating conditions that resulted in a minimized ion beam diameter, or the "optimized condition". A 25,000-step per revolution stepper motor was mounted outside of vacuum and attached to a push/pull feed-through rod. A stainless-steel arm, with the Faraday probe mounted near the end, was attached to the rod and pointed at the ion source. The Faraday probe radial position was adjusted so that its circular path passed through the centerline of the ion beam (+/- 0.5 cm) as shown in Fig. 2. A fine nickel mesh of 75% transparency was placed over the orifice that serves as the entrance to the Faraday probe. The screen and Faraday probe body were biased at -35 V to repel plasma electrons from entering the probe through the orifice. The collector plate located inside the Faraday probe was biased at +20 V to inhibit secondary electron emission and repel low energy ions that might be present in the beam plasma.

In order to characterize the beam, a measurement of current density vs. radial position (R_{beam}) is used (Fig. 3). The raw data from a trace was obtained as current density vs. the angular position of the motor (θ_{arm}). The geometry shown in Figure 2 is used to yield the following relationship:

$$R_{beam} = 2\sin(\theta_{arm}/2)R_{arm} \tag{1}$$

The radial center of the ion beam was defined to coincide with the location of the peak current density. The resulting profiles were fit with sixth order polynomial curve-fits which were subsequently integrated (and corrected for charge exchange losses) to obtain the total beam current flowing from the ion source. In general, the integrated beam currents ($J_{b,int}$) agreed with the indicated beam currents displayed by the power supply (J_b) to within 15%. The analysis of the radial data showed optimized Xe^+ beams (see Table 1) whose full width-at-half-maximum (FWHM) value varied from 2.7 cm to 3 cm. For gases other than Xe, the beam current was adjusted to ensure perveances matched those in Table 1.

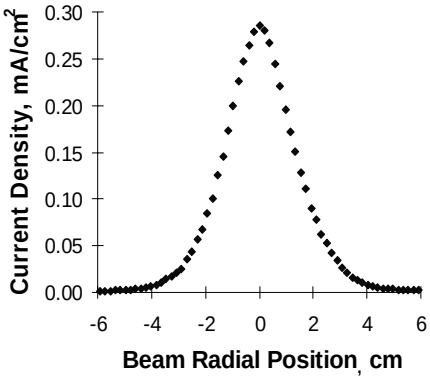

Figure 3. Beam profile for 1000eV Xe^+

The radii within which 90% of the beam current was contained were large enough to put the small beam spot assumption into question. Also, the maximum divergence angle in the low current density (fringe) regions of the ion beam could be as much as 20°, which results in a spread in the actual ion incidence angle. These problems are addressed later in the paper. In the future, a four-grid system design[27] may be beneficial to obtain a divergence of less than 2° and a smaller spot size at lower beam energies.

An ExB probe investigation was performed on a 5 mA, 1000 eV Xe ion beam (xenon having the lowest 2nd ionization potential of the three gases tested) utilizing a discharge voltage of 31 V. The results indicated the doubles-to-singles current ratio was 3.9%, implying that for every 100 singly charged ions in the beam there were ~1.4 doubly charged ions. Note that the doubly charged ions possess twice the energy of their single-charged counterparts, and in the energy regime of interest have roughly twice higher sputter yields. In our analysis, we correct for the presence of doubly charged ions by counting each one as two singly charged ions. Owing to the relatively small number of doubly charged ions and their twice higher yields, such a treatment has a minimal effect on the resulting measured sputter yields. It is noted that for most materials this assumption begins to fail at ion energies below ~150 eV, due to the high sensitivity of sputter yield to energy in this regime.

Table 1. Ion source parameters for smallest diameter beam using Xe^+.

V_b, V	V_a, V	J_b, mA	$J_{b,int}$, mA	FWHM, cm	90% radius, cm
500	-38	1.5	1.27	3.0	3.8
750	-50	2.5	2.29	2.7	4.2
1000	-50	4.0	3.80	2.7	3.5
1500	-100	4.0	3.99	2.9	6.0

C. Quartz Crystal Microbalance (QCM)

The QCM was the device used to measure the differential sputtering distributions. The QCM works by detecting changes in mass on its surface (caused by deposited condensable sputter products) by sensing the change in the crystal's resonant frequency. Each crystal used in these experiments initially resonated at a frequency of ~6 MHz

and had a surface coating of gold to ensure a high initial sticking coefficient. As more mass accumulated on the exposed crystal area, A_s = 0.535 cm^2, the resonant frequency dropped until a resonant frequency of ~5.7 MHz was reached, at which point the crystal was considered un-useable and was replaced. To ensure consistent sticking coefficients for new crystals, a 10μg coating of target material was added before initiating a test. The QCM acceptance angle is 165° and is able to receive a particle from any location on the target.

In general, there are two potential problems[28,29] associated with using QCMs as sputtering measurement devices: 1) measurement instabilities due to thermal changes in the environment and 2) ensuring the QCM sensor face has a uniform flux of particles. We are unaffected by the second problem owing to the inherent set-up of our system, i.e. the QCM position is sufficiently far from the sputtering target to ensure that the arrival flux of sputtered material is spatially uniform. We dealt with the first concern in two ways. The crystal holder was water-cooled at a temperature of ~28°C to accommodate the majority of the thermal stabilization of the system. This temperature value fluctuated approximately 0.1°C every 10 minutes and was considered to have a negligible effect on the mass readings. Due to the movement of the QCM with respect to the ion source and its hot filaments, certain angular locations in the experiment had higher heat fluxes than others. As a result, when the angular position changed, transient heating of the QCM was observed to slightly affect the sputter readings. Therefore, a 70 second long thermal stabilization period was implemented whenever the QCM angular position changed by 10° to further ensure a stable QCM reading.

D. Procedure

The polycrystalline targets used were larger (15.24 cm × 15.24 cm) than the ion beam spot size to ensure that the vast majority of particles bombarded only the target. The targets were cleaned using an acetone solution but were not mechanically polished. Targets were attached to a water cooled copper plate in order to keep the target at a relatively low temperature and minimize out-gassing. The target was leveled in the β = 0° position with an angular accuracy of +/- 1°.

After target preparation, the chamber was evacuated and baked-out for an 8 hour period. Background gases were monitored with an RGA sensitive to species in the 1-100 amu range. In addition, the ion source was set to produce a 1500 eV beam and the target was sputter-cleaned for 1-3 hours. The QCM was held at a fixed α where a moderate amount of deposition would occur so that changes in the differential sputter yield could be monitored as

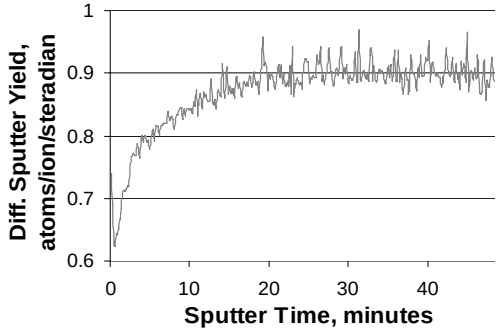

Figure 4. Change in differential sputter yield as the Mo target is sputter cleaned. *Readings were stable after approximately 20 minutes.*

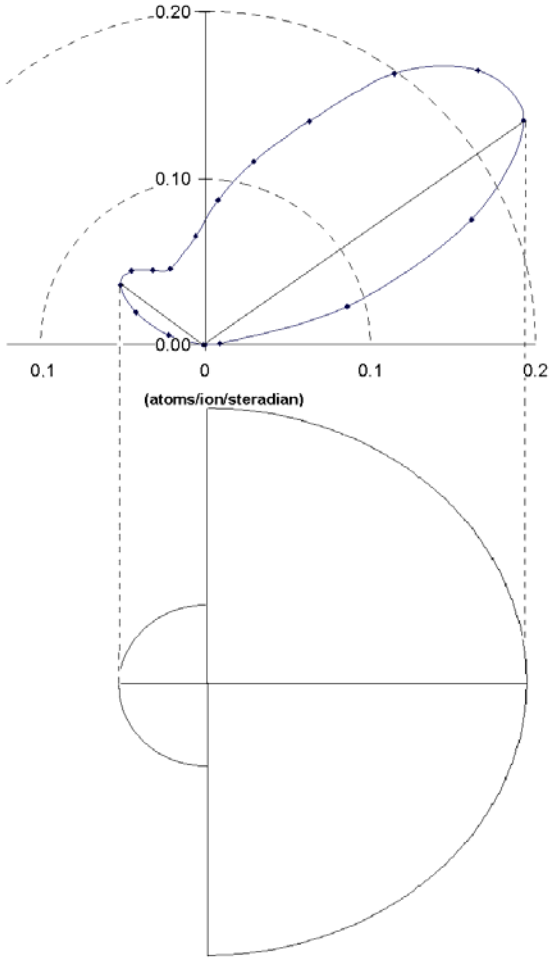

Figure 5. Azimuthal distribution assumption for α = 55°. *Top is a polar plot of the distribution. Bottom is a projection of the distribution into azimuthal components.*

shown in Fig. 4. If this yield reached a stable value at the end of the sputter cleaning period, sputtering tests commenced.

Typically, the QCM was placed at an angle $\alpha = 90°$ and a measurement was taken. The QCM's angular position was then decreased in 10° increments (excluding $\alpha = 0°$ due to beam blockage) until an angle of $\alpha = -90°$ was reached. A typical measurement involved waiting 70 seconds to allow for the thermal stabilization of the QCM followed by 7-10 differential yield measurements; these were averaged to obtain the final reading. If the standard deviation from the averaged value was greater than 5%, the measurement was repeated. A typical differential yield distribution is shown in the top of Fig. 5 for an angle of incidence of 15°, for 500 eV xenon ions on molybdenum. The differential yield measurements were repeated in this way to obtain differential sputter distributions for $\beta = 0°$, 15°, 30°, 45° and 60° for each beam energy of interest (300-1500 eV for Ta, 500-1500 eV for Mo and W), bombarding ion (xenon, argon, and krypton), and target material (molybdenum, tantalum, and tungsten) combination for a total of 185 distributions. Normal incidence sputter yields for Tantalum were extended from the normal 500-1500 eV range to include 150 eV, 200 eV, and 400 eV. If an atmospheric vent was required (to change the target material, replace the QCM crystal, etc.), the bake-out/target cleaning procedure was implemented before differential sputter yield measurements continued.

E. Data Acquisition and Analysis

When the QCM was placed in a polar angular position, α, for a given time, t, the number of sputtered target atoms deposited onto the crystal increases to a value that is proportional to the differential yield. The change in the crystal's frequency is interpreted as a mass reading (in units of μg) by a deposition monitor device. When a differential sputter yield measurement was initiated, the initial QCM mass and initial time were recorded by a LabView program. A delay of several seconds allowed more target atoms to be deposited on the QCM surface. In this delay period, beam current measurements (from the power supply) are taken every 0.5 seconds. At the end of the delay, the final QCM masses and times were recorded in the program to compute the mass accumulation rate, $R(\alpha)$, in g/s. The beam current measurements were averaged to provide $J_{B,avg}$ (C/s). Using the molecular weight of the target atoms (M_t in g/mol), the distance from the target center to the QCM ($r_{qcm} = 17.4$ cm), the QCM sensor area ($A_s = 0.535$ cm^2), the electronic charge ($q = 1.6\times10^{-19}$ C/ion), and Avogadro's number ($N_A = 6.023\times10^{23}$ atoms/mol), a differential yield value can be extracted as shown in Eq. (2):

$$y(\alpha) = \left[R(\alpha)N_A q r_{qcm}{}^2\right] / \left[M_t J_{B,avg} A_s\right] \tag{2}$$

where the term $(r_{qcm}{}^2)/A_s$ provides the solid angle (in steradians) that the QCM sensor subtends, thus giving $y(\alpha)$ units of atoms/ion/steradian.

In order to compare our results to total yield results available in literature, it was necessary to integrate the differential yield results over the hemisphere above the target. As mentioned previously, the differential yield profile was only measured in a single arc above the target for most tests. (Differential sputter yield measurements as a function of both polar and azimuthal angles are discussed in Section III). The arc of $y(\alpha)$ data from $0° < \alpha < 90°$ is defined to correspond to an azimuthal angle (ϕ) of 0° that represents forward sputtered material and $y(\alpha)$ data from $-90° < \alpha < 0°$ is defined to correspond to an azimuthal angle of $\phi = 180°$ that represents back sputtered material. With this method, no additional information is available at different azimuthal angles. Consequently, an assumption was made that the forward sputtered distributions are uniform over the range of ϕ from $-90° < \phi < 90°$, and back sputtered distributions are uniform over the range of ϕ from $90° < \phi < 270°$ (see Fig. 5). This symmetry assumption allows one to integrate our differential sputter yield distributions to obtain the total sputter yield as shown in Eq. (3).

$$Y = \int_0^{2\pi}\left(\int_0^{\pi/2} 2\pi \sin(\alpha) y(\alpha,\phi) d\alpha\right) d\phi \tag{3}$$

The differential yield data was first fit using two sixth-order polynomial curve-fittings according to Eqs. (4) and (5) after $y(\alpha)$ was plotted versus $\cos(\alpha)$[4,5]. One curve-fit was applied to the differential yields in the forward sputtered direction (A coefficients), and the other was fit to the back sputtered direction (B coefficients). The A and B coefficients obtained from all of our measurements are available in Appendix 1. Using the azimuthal distribution assumption described, Eq. (3) is reduced to Eq. (6). While the aforementioned assumption on the azimuthal

behavior is not physically correct for non-normal incidence, it provides a practical means of determining total sputter yields, and gives values that agree reasonably well with published yields.

$$y(0 \le \alpha \le 90) = A_6 \cos^6(\alpha) + A_5 \cos^5(\alpha) + \ldots + A_1 \cos(\alpha) \tag{4}$$

$$y(-90 \le \alpha \le 0) = B_6 \cos^6(\alpha) + B_5 \cos^5(\alpha) + \ldots + B_1 \cos(\alpha) \tag{5}$$

$$Y = \sum_{i=1}^{6} \frac{\pi}{i+1} A_i + \sum_{i=1}^{6} \frac{\pi}{i+1} B_i \tag{6}$$

III. Results Comparison and Discussion

Due to the large number of tests, all results are reported in Appendix 1 in tabular form to save space. This section features the comparisons of *some* of our results to other research groups and shows typical differential sputtering distributions. The first section contains sputtering results measured at normal incidence (where the bulk of the sputtering data has been obtained in the literature). A second section contains sputtering results at off-normal (oblique) incidence, and a final section analyzes the validity of the major assumptions used in our investigation.

A. Normal Incidence

At normal incidence, the forward and backward distributions were found to be very similar, which supports our symmetry assumption for normal incidence and provides a rough check on the data. Figures 6 and 7 compare our QCM-based sputtering distributions to groups[6,7] using RBS measurement techniques performed on semi-circular foil collector strips that are exposed to materials sputtered from a target located below the foil. The distributions shown have a distinctive under-cosine shape typical of the low energy xenon sputtering regime of most materials. Our *y(α)* distributions measured in the forward direction were very similar to those recorded by Shutthanandan (Fig. 7), however, our magnitudes were about 30% lower. Due to our lower *total* yield measurements (discussed below) for molybdenum at normal incidence, it is likely that Shutthanandan's measurements have more accurate distribution

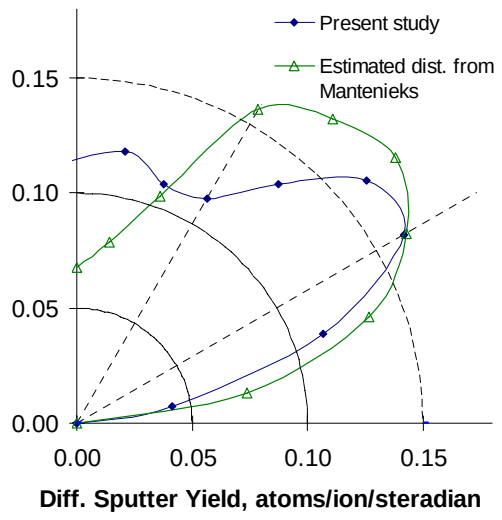

Figure 6. Polar plot of the differential sputtering yields for Xe^+ on Ta at 500 eV at normal incidence.

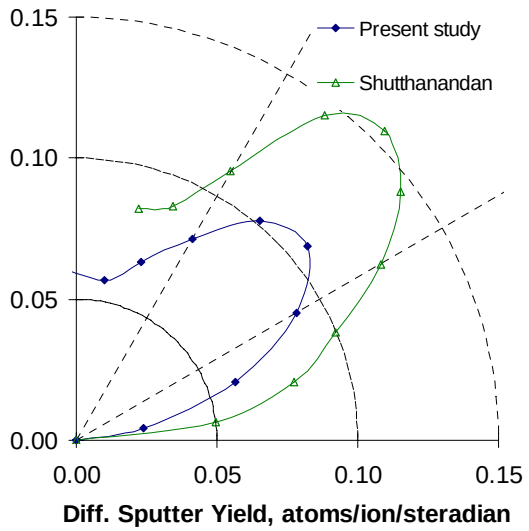

Figure 7. Polar plot of the differential sputtering yields for Xe^+ on Mo at 500 eV at normal incidence.

magnitudes. When compared to a distribution measured by Mantenieks (Fig. 6), our magnitudes were similar although our distribution shape was quite different from $\alpha = 0°$ to 40°.

Figures 8 through 13 compare some of our integrated (normal incidence) total sputter yields with data from other groups[6,7,30-33]. Our total yields were lower than most other experimentally obtained sputter yields, although good agreement to Yamamura and Tawara curve fits[30] was observed.

The distributions about the $\alpha = 0°$ axis were expected and observed (within a few percent) to be symmetric in most of the normal incidence cases. In the distributions where symmetry was not observed, a slight deviation from target level was detected after the test, thereby indicating high sensitivity of distribution shapes to the angle of incidence near $\beta = 0°$.

For each distribution, as the energy of the bombarding ion is increased, the distribution at normal incidence becomes less under-cosine and more cosine or over-cosine[4,5]. For all Z ratios (Z_{ion}/Z_{target}) investigated in this study, the distributions at 1000 eV for normal incidence had either cosine or over-cosine distributions. For all Z ratios greater than 0.5, the distributions at 500 eV had clear under-cosine shapes at normal incidence. This implied that the collision cascades at these conditions did not produce many sputtered atoms with energies greater than the surface binding energy that were ejected in the direction normal to the target. For Ar^+ on Ta and W (Z ratio ~0.24) at 500 eV the distributions were nearly cosine.

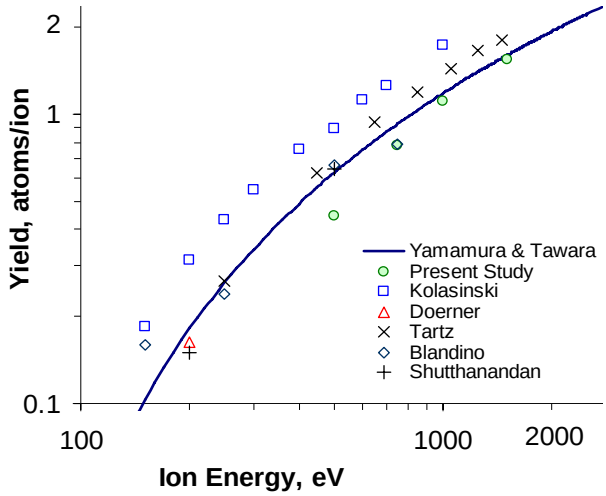

Figure 8. Total yields for Xe^+ on Mo.

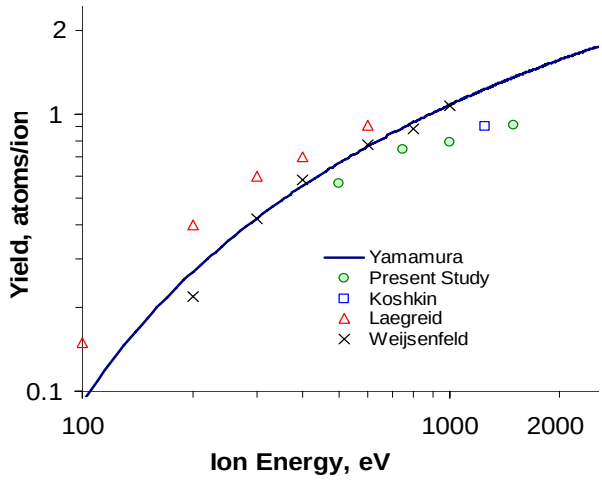

Figure 9. Total yields for Ar^+ on Mo

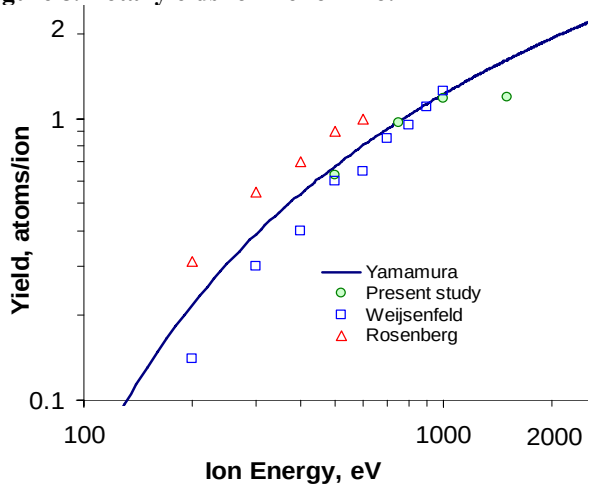

Figure 10. Total yields for Kr^+ on Mo.

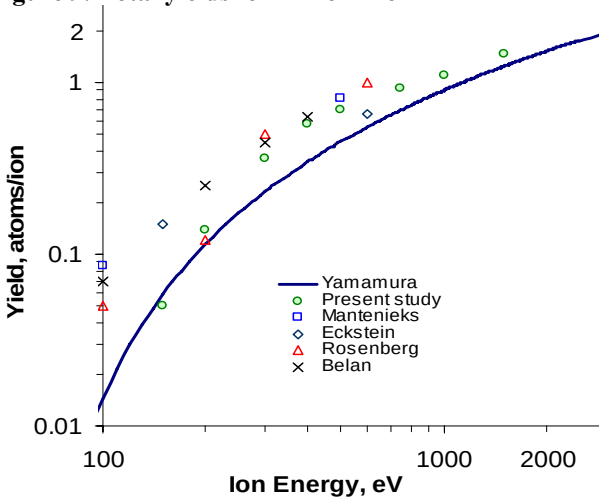

Figure 11. Total yields for Xe^+ on Ta.

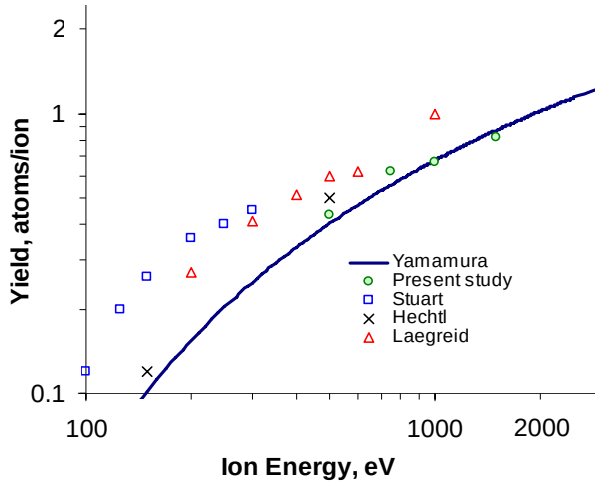

Figure 12. Total yields for Ar^+ on Ta.

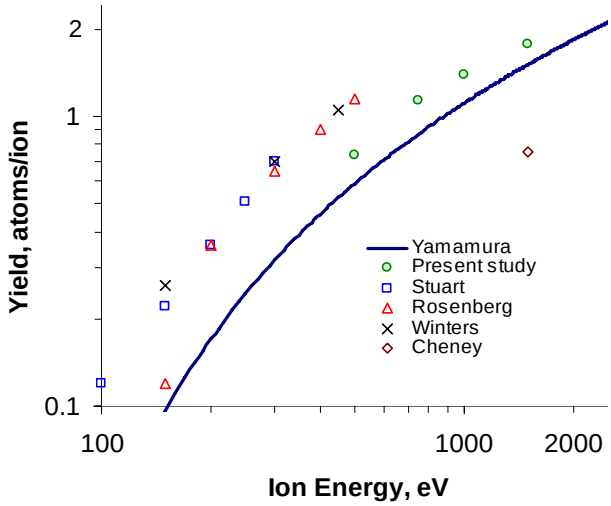

Figure 13. Total yields for Xe+ on W.

B. Non-Normal Incidence

Figures 14 and 15 compare total yield data calculated from differential yield measurements to those measured by various groups[23,24] for oblique incidence conditions. Again, our total sputtering yields are shown to be lower than those of other groups. However, the initial rates of rise of each group's results in both figures are almost identical. Tartz shows a maximum yield occurring at an angle of incidence of 60°-70° in Fig. 14, while both Kolasinski's and our results have maxima in the 50°- 60° range.

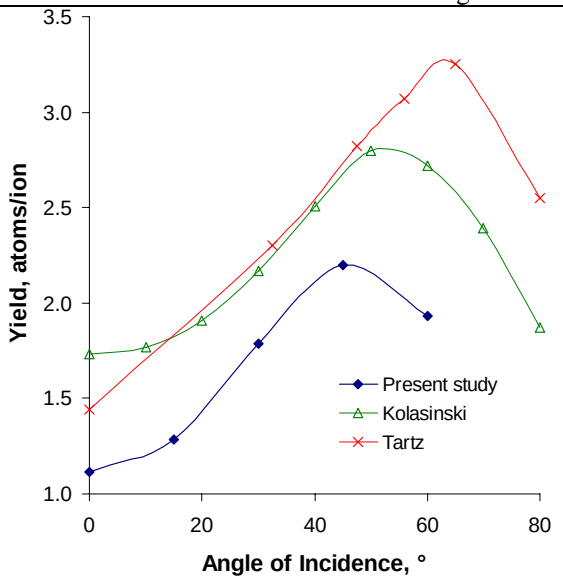

Figure 14. Sputter yield vs. angle of incidence for 1000 eV Xe^+ on Mo.

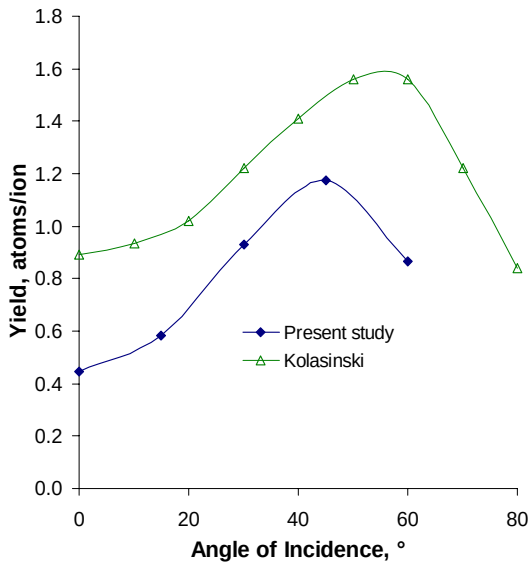

Figure 15. Sputter yield vs. angle of incidence for 500 eV Xe^+ on Mo.

For the distributions where the *Z* ratio was greater than 0.5 (i.e., for Xe^+ on Mo, Ta, and W and Kr^+ on Mo), 500 and 750 eV ions caused more material to be forward sputtered as the angle of incidence was increased from 15° to 45° (see Fig. 16 for 500 eV data). At a higher incidence angle of 60°, less forward sputtering and more back sputtering was observed, which gave the distributions a more rounded shape. When the *Z* ratio was less than 0.5 (see Fig. 17) at ion energies of 500 and 750 eV, we witnessed a similar trend, but the distributions were noticeably broader. At higher energies (1000 eV and 1500 eV), we observed more broadening of the distributions and a definite shift toward over-cosine behavior at all incidence angles when $Z < 0.5$ (e.g., see Figs. 18 and 19 for 1500 eV data). This same behavior was seen with Ar^+ on W at all angles of incidence. In general, as the beam energy was increased, distributions at all angles of incidence approached a cosine or over-cosine distribution.

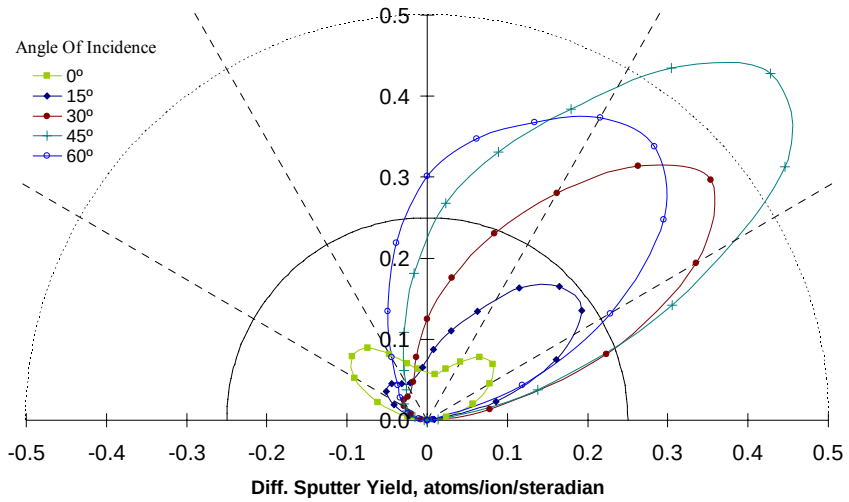

Figure 16. Differential yield distributions at varying angles of incidence for 500 eV Xe^+ on Mo. ***Typical of Z ratio > 0.5 results at low energy.***

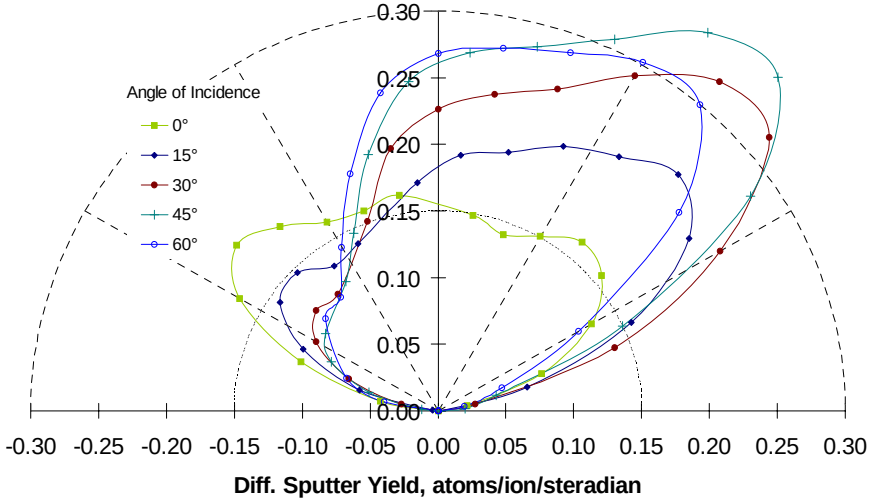

Figure 17. Differential yield distributions at varying angles of incidence for 500 eV Kr^+ on W. ***Typical of Z ratio < 0.5 results at low energy.***

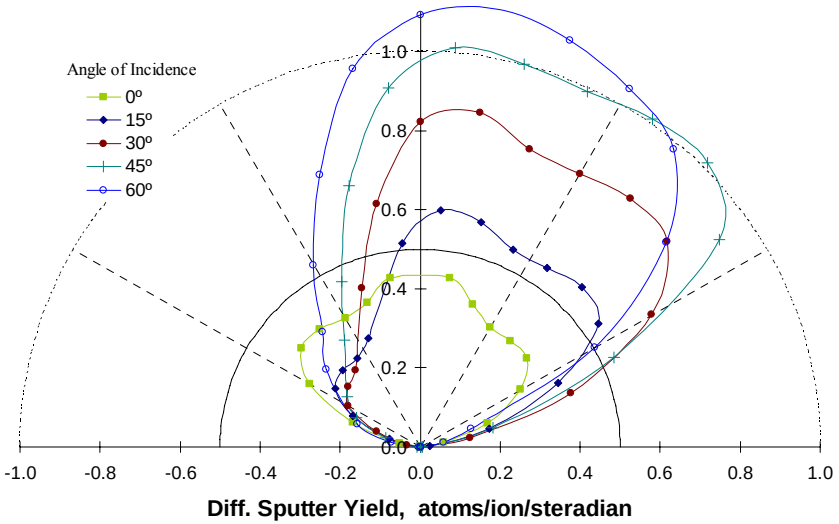

Figure 18. Differential yield distributions at varying angles of incidence for 1500 eV Xe^+ on Mo. ***Typical of Z ratio > 0.5 results at high energy.***

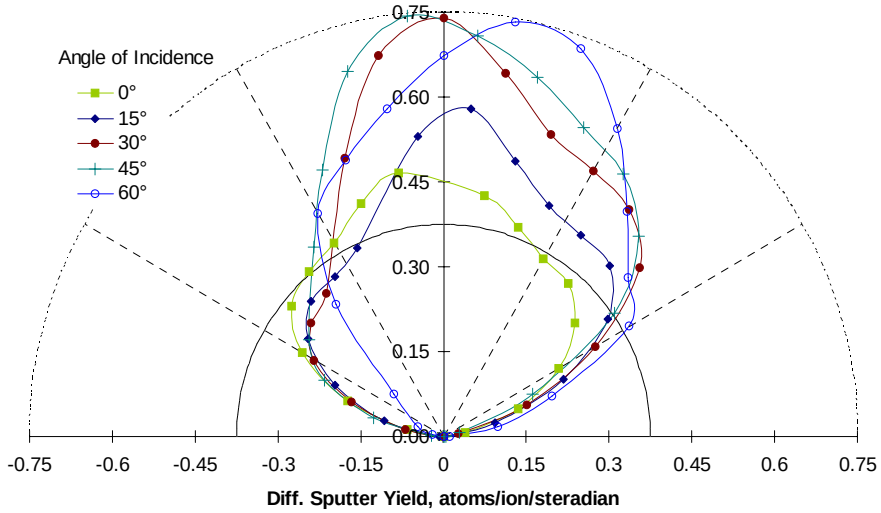

Figure 19. Differential yield distributions at varying angles of incidence for 1500 eV Kr^+ on W. ***Typical of Z ratio < 0.5 results at high energy.***

C. Analyses of Major Assumptions

1. Large Beam Spot Analysis

The potential problems relating to the aforementioned assumptions on ion beam spot-size and divergence angles called for further investigation into the sensitivity of the measured sputter yield profile to these effects. A simple computer model of the sputtering of the target was created by representing the beam spot on the target as a set of nodes. Using the Faraday probe traces, each node was assigned an ion flux based on its radial position in the beam. A local angle of incidence was also calculated for each node based on the target tilt and the divergence angle of the ion beam at that node. Using the experimental differential yield distributions, an interpolated differential yield distribution was assigned to each node based on its local angle of incidence. A simulated QCM sensor was placed at differing polar angles and then the flux of atoms to that sensor was calculated and a differential yield extracted. Results in Fig. 20 show that for the worst case scenario of a 1500 eV beam, most differential yield measurements were found to be in acceptable agreement with the experiment. There seemed to be two polar angle regions (α = 0° and 45°) where there was a difference of approximately 5%. The simulated differential sputter distribution values were typically less than the measured distribution values.

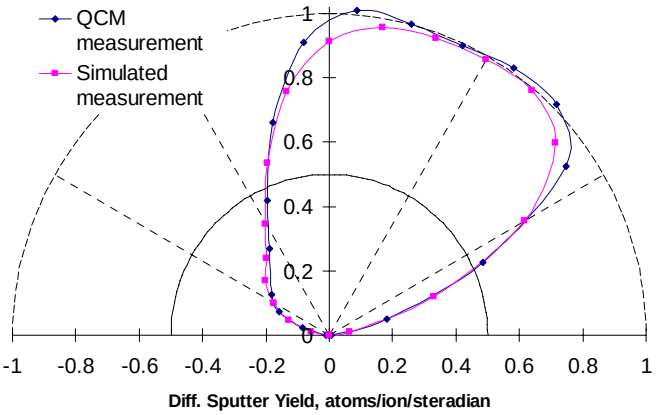

Figure 20. Actual QCM measurement vs. a simulated measurement for 1500 eV Xe^+ on Mo at β = 45°. *The simulation accounts for a large beam spot size and differing angles of incidence due to beam divergence.*

2. Azimuthal Assumption Analysis

The assumed azimuthal sputtering distribution described above was noted as not being physically realistic for oblique incidence. Computer simulations using TRIM indicated a fairly symmetric azimuthal distribution even in cases where oblique angles of incidence were used, which was not observed in our single plane azimuthal measurement. A preliminary experimental investigation was devised to obtain sputter yield data at multiple azimuthal angles as shown in Fig. 21. The design of the QCM hardware constrained its swept path to lie on a single arc for a given azimuthal angle. Therefore, we achieve measurements at multiple azimuthal angles by (azimuthally) rotating the target fixture (as opposed to the detector). The fixture, shown on the left in Fig. 22, consists of a base plate, an adjustable arm holding the target at a height where the QCM's view was centered, and a target mount allowing rotation of the target (thus specifying both the angle of ion incidence and the azimuthal angle to the detector). The base plate and target were made of molybdenum, while the arm and mount were made of stainless-steel. The target was sufficiently large to prevent any of the components beneath it from exposure to the ion beam.

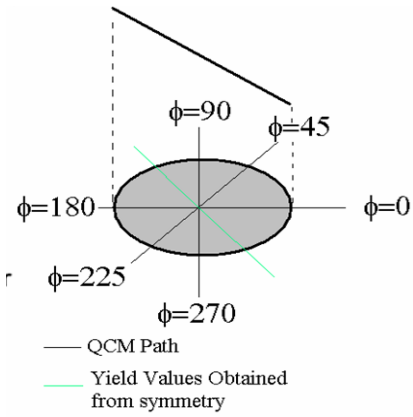

Figure 21. Definition of angle ϕ.

Figure 21 defines the angles used in the experiments. We referred to the azimuthal angle of the QCM's path from the plane defined by the ion beam and target normal direction as ϕ. Before each measurement, the target was aligned to ensure correct height, angle of incidence, and azimuthal angle. Of these alignment variables, the azimuthal angle had the highest degree of uncertainty (+/- 5°). Once aligned, the test chamber was evacuated, baked out, and the target was sputter cleaned for 3 hours to remove any surface contaminants on the target. In order to rotate the target fixture to change the azimuthal angle, a vent to atmosphere was required between each azimuthal test (after which the above alignment/cleaning sequence is repeated). For the data shown here, measurements for α =

-90° to 90° (corresponding to one sweep of the QCM) were taken at: β = 0°, 15°, and 30° (i.e. three incidence angles) for ϕ = 0°, 45°, and 90°.

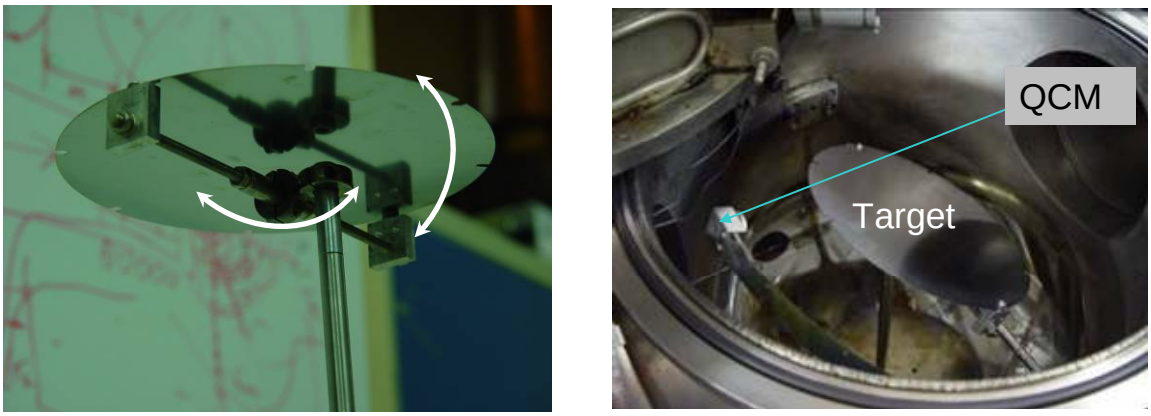

Figure 22. *Left: Target fixture showing target, mount, and top portion of the arm. Right: Target fixture and QCM.*

Results of differential sputter yield measurements for molybdenum for β = 15° are shown in Fig. 23. The data show that the highest amount of sputtering occurs in the ϕ = 0°, α = 45° direction. This was expected, as this was the azimuthal direction of the target tilt, i.e. ϕ = 0 corresponded to "forward sputtering of material". For polar angle α = 0°, the azimuthal angle became degenerate (i.e. all ϕ correspond to the same geometry for α = 0°) so that comparing the measured rates at α = 0 provided a check on the data; indeed, the measured sputter yields were the same (within error) at α = 0 as anticipated. Another expected result was that the differential sputter yields for ϕ = 90° are symmetric in α (with respect to α = 0), owing to the corresponding symmetry in the sputtering geometry. A somewhat surprising result was the differential yields for α = 0° to -90° were almost identical for ϕ = 0° and 45°. It was thought that the values for ϕ = 45° would lie somewhere between those of ϕ = 0° and ϕ = 90°. The right of Fig. 23 shows a contour polar plot of the distributions, with the angles shown representing ϕ while the contours are for different α.

Results of differential sputter yield measurements for molybdenum for β = 30° are shown in Fig. 24. The data again show that the highest amount of sputtering occurred at the expected ϕ = 0°, α = 45° direction. In this case the data points near α = 0 for ϕ = 0° and 45° have nearly the same magnitude; however for ϕ = 90° the magnitude is about half that of ϕ = 0° and 45°. As explained above, one expected these values (i.e. for α = 0°) to be uniform. The inconsistency for ϕ = 90° is likely indicative of a problem in the measurement system and is being investigated in our ongoing work. In contrast to the β = 15° case, here we see that in the α = 0° to -90°, the distribution for ϕ = 45° lies in between the ϕ = 0° and 90° distribution, which was expected. The right of Fig. 24 shows a contour polar plot of the distributions, with the angles shown representing ϕ while the contours are for different α.

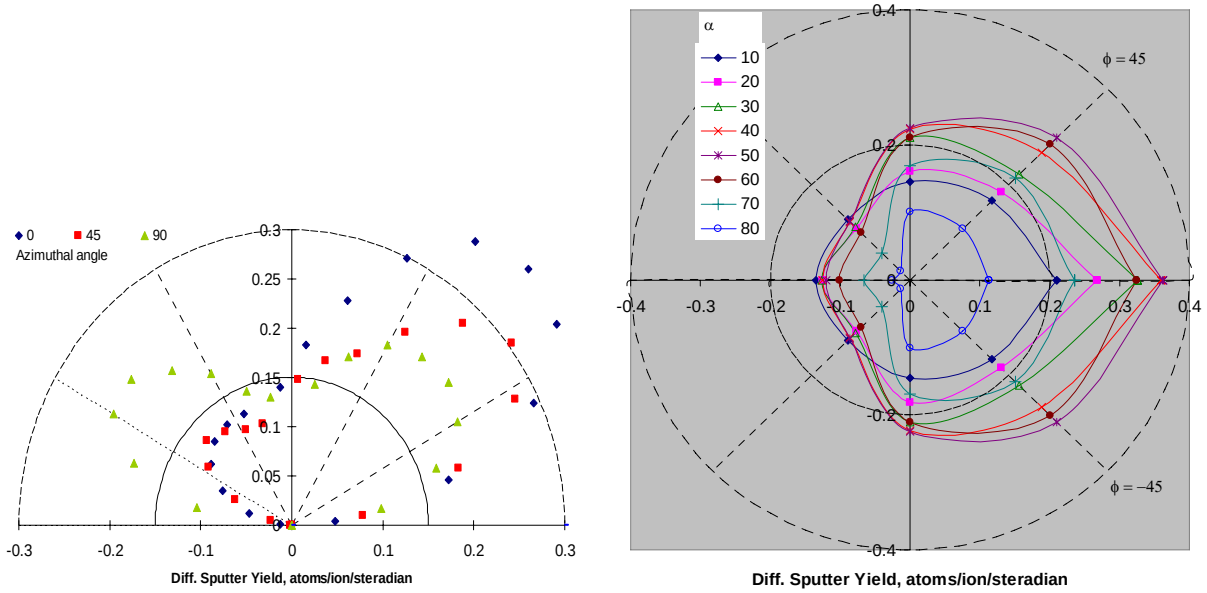

Figure 23. *Left: Differential yield distributions for Mo (as function of α) at varying azimuthal angles (ϕ=0,45,90°) for β = 15°. Right: Contour polar plot of differential yield distributions for β = 15°. Polar angle is ϕ, while the contours are for different α.*

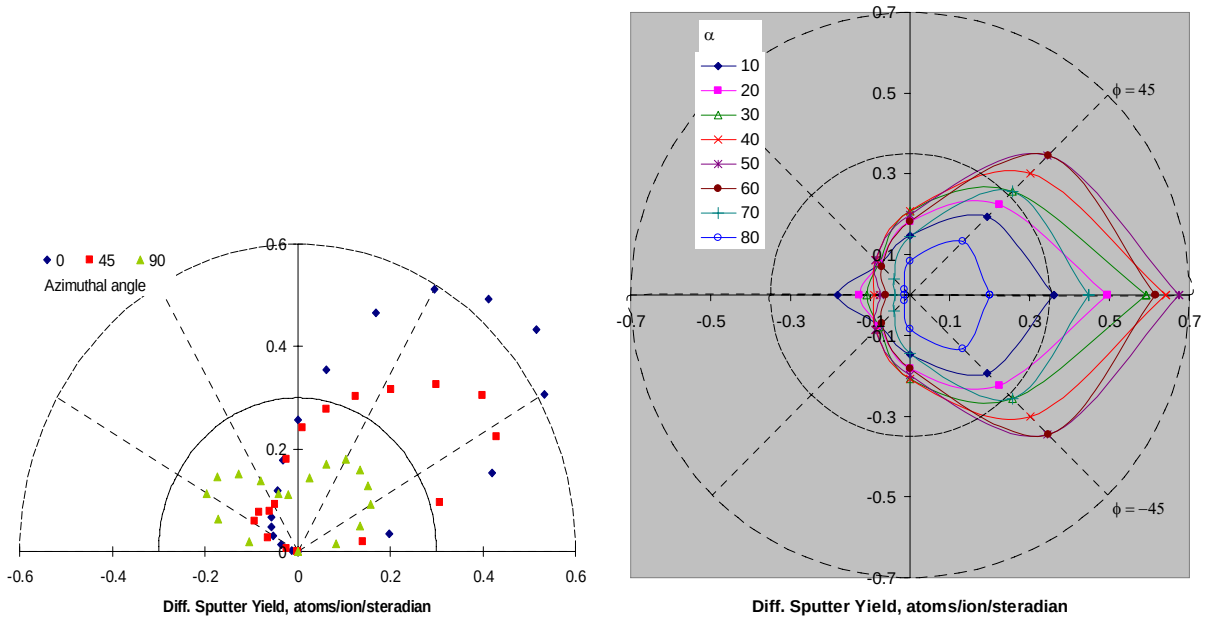

Figure 24. *Left: Differential yield distributions for Mo (as function of α) at varying azimuthal angles (ϕ=0,45,90°) for β = 30°. Right: Contour polar plot of differential yield distributions for β = 30°. Polar angle is ϕ, while the contours are for different α.*

IV. Conclusions

A QCM based technique has been used to obtain differential sputtering yield distributions in a single azimuthal plane for ion and target combinations of interest to the EP community. Angles of incidence investigated were 0°, 15°, 30°, 45°, and 60° and bombarding ion energies were from 150 eV to 1500 eV. All distributions obtained are tabulated in Appendix 1. The differential yield distributions were integrated using a simple azimuthal assumption to obtain total sputter yields and compared to values of other researchers. Our total yields were generally lower than, but comparable to, other experimental values. Comparisons of the full distributions to those measured by other research groups have shown satisfactory agreement. Our total yields, as a function of angle of incidence, were also lower than other researchers, but initial rates of rise seem to agree.

Our measurements show that at 1000 eV and 1500 eV, differential yield distributions at angles of incidence below 60° approach an over-cosine or cosine shape. At lower energy (<800 eV), it was observed that less material was sputtered in the $\alpha = 0°$ region than in the higher energy cases. Distributions for ion and target combinations with a Z ratio less than 0.5 were found to be nearly cosine for lower energies and became over-cosine as the energy increased. Also, at low energies, for ion and target combinations having a Z ratio greater than 0.5, a majority of particles were sputtering in $\alpha = +30°$ to $+60°$ directions, while at high energies these combinations approached a more cosine-like distribution.

Analyses of two major assumptions in our experiments were conducted. A simulation was done to investigate the effects of the large divergence and beam spot-size on our differential yield results. The simulations indicated there is a small (5%) discrepancy between measured and simulated QCM values for polar angles near $\alpha = 0°$ and near $\alpha = 45°$, with smaller discrepancies at other polar angles. A preliminary investigation into the azimuthal assumption was also conducted.

Future work will include measuring sputtering distributions at lower energies (owing to their importance to EP), and modifying the azimuthal sputter distribution experiment to reduce or eliminate the need to break chamber vacuum.

Appendix 1. Coefficients of Differential Sputtering Yield Curve Fits

These tables can be used to obtain Cartesian graphs of $y(\alpha)$ vs. $\cos(\alpha)$ for α = -90° to 90°.

E (eV)	β °	Target	Ion	Y (atoms/ion)	A6	A5	A4	A3	A2	A1	B6	B5	B4	B3	B2	B1
500	0	Mo	Xe	0.44	1.950E+00	-4.833E+00	4.486E+00	-2.455E+00	8.638E-01	4.444E-02	4.709E-01	-3.232E-01	-6.052E-01	-3.311E-03	4.538E-01	6.405E-02
500	15	Mo	Xe	0.58	-2.636E-01	1.291E+00	-7.020E-01	-2.372E+00	2.198E+00	-6.454E-02	4.348E+00	-1.097E+01	1.065E+01	-5.404E+00	1.539E+00	-8.864E-02
500	30	Mo	Xe	0.93	-2.172E+01	6.951E+01	-8.244E+01	4.175E+01	-7.904E+00	9.483E-01	1.708E+01	-4.719E+01	4.943E+01	-2.445E+01	5.669E+00	-4.241E-01
500	45	Mo	Xe	1.18	8.810E-01	5.443E+00	-1.575E+01	9.647E+00	-9.676E-02	1.469E-01	3.225E+01	-8.609E+01	8.501E+01	-3.787E+01	7.324E+00	-3.952E-01
500	60	Mo	Xe	0.87	-4.114E+00	1.110E+01	-1.122E+01	2.931E+00	1.945E+00	-3.322E-01	4.011E+01	-1.163E+02	1.280E+02	-6.544E+01	1.515E+01	-1.166E+00
750	0	Mo	Xe	0.78	4.194E+00	-8.863E+00	6.375E+00	-2.672E+00	1.023E+00	1.028E-01	7.239E+00	-1.774E+01	1.603E+01	-7.838E+00	2.604E+00	-1.318E-01
750	15	Mo	Xe	1.16	-2.288E+01	6.786E+01	-7.472E+01	3.784E+01	-1.008E+01	2.176E+00	5.272E+00	-1.298E+01	1.261E+01	-6.950E+00	2.355E+00	-1.481E-01
750	30	Mo	Xe	1.51	-3.703E+01	1.219E+02	-1.483E+02	7.821E+01	-1.625E+01	1.820E+00	3.398E+01	-9.304E+01	9.715E+01	-4.836E+01	1.147E+01	-8.835E-01
750	45	Mo	Xe	1.91	-4.661E+00	3.113E+01	-5.405E+01	3.219E+01	-4.675E+00	6.326E-01	5.354E+01	-1.424E+02	1.411E+02	-6.377E+01	1.286E+01	-7.495E-01
750	60	Mo	Xe	1.52	-2.708E+01	9.619E+01	-1.312E+02	8.160E+01	-2.102E+01	2.083E+00	5.403E+01	-1.553E+02	1.703E+02	-8.740E+01	2.049E+01	-1.496E+00
1000	0	Mo	Xe	1.11	-6.441E-01	7.248E+00	-1.267E+01	6.933E+00	-9.362E-01	3.491E-01	4.790E+00	-7.530E+00	2.057E+00	-1.656E-01	1.116E+00	1.118E-02
1000	15	Mo	Xe	1.29	-5.631E+00	2.207E+01	-2.805E+01	1.200E+01	-2.199E-01	1.949E-01	1.401E+01	-3.272E+01	2.868E+01	-1.300E+01	3.590E+00	-2.142E-01
1000	30	Mo	Xe	1.79	-2.275E+01	7.709E+01	-9.464E+01	4.825E+01	-8.636E+00	1.216E+00	5.242E+01	-1.450E+02	1.533E+02	-7.723E+01	1.851E+01	-1.448E+00
1000	45	Mo	Xe	2.20	-1.427E+01	5.896E+01	-8.362E+01	4.614E+01	-7.220E+00	7.426E-01	5.390E+01	-1.428E+02	1.419E+02	-6.503E+01	1.353E+01	-7.752E-01
1000	60	Mo	Xe	1.93	-4.098E+01	1.393E+02	-1.800E+02	1.050E+02	-2.460E+01	2.045E+00	4.209E+01	-1.193E+02	1.305E+02	-6.762E+01	1.629E+01	-1.155E+00
1500	0	Mo	Xe	1.54	2.096E+00	2.436E-01	-5.135E+00	2.250E+00	8.472E-01	1.591E-01	3.959E+00	-4.067E+00	-1.854E+00	8.900E-01	1.509E+00	2.013E-02
1500	15	Mo	Xe	1.78	-7.314E+00	2.854E+01	-3.578E+01	1.534E+01	-4.431E-01	2.599E-01	2.098E+01	-4.945E+01	4.406E+01	-2.018E+01	5.478E+00	-3.114E-01
1500	30	Mo	Xe	2.26	-1.584E+01	5.562E+01	-6.759E+01	3.146E+01	-3.504E+00	7.022E-01	5.991E+01	-1.603E+02	1.642E+02	-8.103E+01	1.953E+01	-1.495E+00
1500	45	Mo	Xe	2.62	-1.374E+01	5.837E+01	-8.232E+01	4.384E+01	-5.468E+00	3.340E-01	5.846E+01	-1.540E+02	1.532E+02	-7.135E+01	1.547E+01	-8.660E-01
1500	60	Mo	Xe	2.54	-5.716E+01	2.002E+02	-2.672E+02	1.638E+02	-4.263E+01	4.033E+00	3.848E+01	-1.073E+02	1.166E+02	-6.057E+01	1.471E+01	-8.290E-01

$$y(\alpha) = A_6 \cos^6(\alpha) + A_5 \cos^5(\alpha) + A_4 \cos^4(\alpha) + A_3 \cos^3(\alpha) + A_2 \cos^2(\alpha) + A_1 \cos(\alpha) \qquad 0^o \le \alpha < 90^o$$

$$y(\alpha) = B_6 \cos^6(\alpha) + B_5 \cos^5(\alpha) + B_4 \cos^4(\alpha) + B_3 \cos^3(\alpha) + B_2 \cos^2(\alpha) + B_1 \cos(\alpha) \qquad -90^o \le \alpha < 0^o$$

$$Y = \sum_{i=1}^{6} \frac{\pi}{i+1} A_i + \sum_{i=1}^{6} \frac{\pi}{i+1} B_i$$

E (eV)	β °	Target	Ion	Y (atoms/ion)	A6	A5	A4	A3	A2	A1	B6	B5	B4	B3	B2	B1
500	0	Mo	Ar	0.56	0.000E+00	1.288E+00	-2.632E+00	1.336E+00	2.257E-02	1.199E-01	0.000E+00	1.655E+00	-3.545E+00	2.043E+00	-1.114E-01	9.684E-02
500	15	Mo	Ar	0.68	0.000E+00	-1.776E-01	1.572E+00	-3.272E+00	2.099E+00	-5.359E-02	0.000E+00	1.533E+00	-2.841E+00	1.207E+00	2.333E-01	1.718E-02
500	30	Mo	Ar	0.81	-8.962E+00	2.622E+01	-2.809E+01	1.213E+01	-1.409E+00	3.094E-01	0.000E+00	2.082E+00	-4.042E+00	2.308E+00	-2.548E-01	7.418E-02
500	45	Mo	Ar	0.93	-1.109E+01	3.353E+01	-3.631E+01	1.481E+01	-7.887E-01	9.403E-02	0.000E+00	1.656E+00	-2.537E+00	7.969E-01	2.482E-01	3.488E-02
500	60	Mo	Ar	0.77	-1.071E+01	3.463E+01	-4.257E+01	2.262E+01	-4.028E+00	2.719E-01	0.000E+00	1.713E+00	-3.134E+00	1.791E+00	-3.175E-01	1.319E-01
750	0	Mo	Ar	0.75	0.000E+00	1.073E+00	-1.856E+00	4.112E-01	4.664E-01	1.028E-01	0.000E+00	1.759E+00	-3.631E+00	1.863E+00	9.967E-02	1.086E-01
750	15	Mo	Ar	0.87	0.000E+00	-3.355E-01	2.122E+00	-3.893E+00	2.399E+00	-4.433E-02	0.000E+00	2.172E+00	-3.727E+00	1.253E+00	5.280E-01	-2.156E-03
750	30	Mo	Ar	1.01	-6.692E+00	1.863E+01	-1.838E+01	6.313E+00	2.926E-01	1.456E-01	0.000E+00	3.206E+00	-6.244E+00	3.710E+00	-5.488E-01	1.429E-01
750	45	Mo	Ar	1.07	-1.323E+01	4.098E+01	-4.651E+01	2.177E+01	-2.944E+00	2.690E-01	0.000E+00	1.812E+00	-2.501E+00	3.386E-01	6.329E-01	1.391E-02
750	60	Mo	Ar	0.92	-2.156E+01	7.506E+01	-1.005E+02	6.206E+01	-1.630E+01	1.538E+00	0.000E+00	1.897E+00	-3.098E+00	1.287E+00	3.009E-02	1.621E-01
1000	0	Mo	Ar	0.80	0.000E+00	7.994E-01	-1.443E+00	2.263E-01	5.563E-01	7.594E-02	0.000E+00	8.683E-01	-1.642E+00	3.260E-01	6.022E-01	6.043E-02
1000	15	Mo	Ar	0.94	0.000E+00	-1.005E+00	3.768E+00	-5.321E+00	2.970E+00	-1.318E-01	0.000E+00	1.992E+00	-3.392E+00	1.082E+00	5.421E-01	2.689E-02
1000	30	Mo	Ar	1.05	-1.150E+01	3.262E+01	-3.302E+01	1.277E+01	-6.441E-01	9.774E-02	0.000E+00	2.382E+00	-3.889E+00	1.313E+00	4.608E-01	3.044E-02
1000	45	Mo	Ar	1.14	-8.713E+00	2.767E+01	-3.192E+01	1.457E+01	-1.320E+00	1.075E-01	0.000E+00	1.476E+00	-1.741E+00	-1.662E-01	7.334E-01	4.789E-02
1000	60	Mo	Ar	0.97	-1.133E+01	4.197E+01	-6.015E+01	3.959E+01	-1.082E+01	1.080E+00	0.000E+00	1.793E+00	-3.047E+00	1.322E+00	1.951E-02	2.168E-01
1500	0	Mo	Ar	0.92	0.000E+00	-1.452E+00	3.796E+00	-3.992E+00	1.888E+00	-1.459E-03	0.000E+00	8.425E-02	3.934E-01	-1.543E+00	1.349E+00	-2.469E-02
1500	15	Mo	Ar	1.06	0.000E+00	-1.399E+00	4.581E+00	-5.782E+00	2.979E+00	-5.366E-02	0.000E+00	1.804E+00	-3.105E+00	9.043E-01	6.707E-01	1.131E-02
1500	30	Mo	Ar	1.13	-4.576E+00	1.055E+01	-5.840E+00	-3.255E+00	3.864E+00	-3.699E-01	0.000E+00	4.686E+00	-9.479E+00	5.966E+00	-1.017E+00	1.934E-01
1500	45	Mo	Ar	1.20	-4.207E+00	1.326E+01	-1.394E+01	3.730E+00	1.890E+00	-3.072E-01	0.000E+00	7.591E-01	-9.618E-03	-1.802E+00	1.482E+00	-3.026E-02
1500	60	Mo	Ar	1.07	1.219E+01	-3.108E+01	2.416E+01	-4.363E+00	-8.211E-01	2.963E-01	0.000E+00	1.468E+00	-2.682E+00	1.531E+00	-3.012E-01	3.472E-01

$$y(\alpha) = A_6 \cos^6(\alpha) + A_5 \cos^5(\alpha) + A_4 \cos^4(\alpha) + A_3 \cos^3(\alpha) + A_2 \cos^2(\alpha) + A_1 \cos(\alpha) \qquad 0^o \le \alpha < 90^o$$

$$y(\alpha) = B_6 \cos^6(\alpha) + B_5 \cos^5(\alpha) + B_4 \cos^4(\alpha) + B_3 \cos^3(\alpha) + B_2 \cos^2(\alpha) + B_1 \cos(\alpha) \qquad -90^o \le \alpha < 0^o$$

$$Y = \sum_{i=1}^{6} \frac{\pi}{i+1} A_i + \sum_{i=1}^{6} \frac{\pi}{i+1} B_i$$

E (eV)	β °	Target	Ion	Y (atoms/ion)	A6	A5	A4	A3	A2	A1	B6	B5	B4	B3	B2	B1
500	0	Mo	Kr	0.63	-5.025E+00	1.976E+01	-2.688E+01	1.523E+01	-3.444E+00	4.467E-01	-8.858E+00	2.981E+01	-3.671E+01	1.927E+01	-3.929E+00	4.945E-01
500	15	Mo	Kr	0.75	6.500E+00	-1.500E+01	1.252E+01	-6.709E+00	2.974E+00	-1.529E-01	6.182E+00	-1.466E+01	1.332E+01	-6.588E+00	1.915E+00	-4.766E-02
500	30	Mo	Kr	1.01	2.923E-01	7.109E+00	-1.739E+01	1.115E+01	-1.268E+00	3.158E-01	1.926E+01	-5.146E+01	5.254E+01	-2.571E+01	5.933E+00	-3.711E-01
500	45	Mo	Kr	1.26	1.308E+01	-2.598E+01	1.351E+01	-2.587E+00	2.416E+00	-1.059E-01	3.300E+01	-8.815E+01	8.754E+01	-3.943E+01	7.682E+00	-3.548E-01
500	60	Mo	Kr	1.00	-7.699E+00	3.278E+01	-5.122E+01	3.358E+01	-7.822E+00	7.007E-01	3.300E+01	-9.518E+01	1.043E+02	-5.299E+01	1.206E+01	-8.383E-01
750	0	Mo	Kr	0.97	1.503E+01	-4.101E+01	4.320E+01	-2.310E+01	6.530E+00	-4.259E-01	-7.959E+00	3.060E+01	-4.075E+01	2.200E+01	-4.189E+00	5.101E-01
750	15	Mo	Kr	1.11	2.799E+01	-7.529E+01	7.603E+01	-3.816E+01	1.037E+01	-6.691E-01	1.074E+01	-2.528E+01	2.301E+01	-1.144E+01	3.395E+00	-1.594E-01
750	30	Mo	Kr	1.42	-2.644E+01	8.551E+01	-1.027E+02	5.317E+01	-1.027E+01	1.099E+00	2.247E+01	-5.971E+01	6.154E+01	-3.131E+01	7.920E+00	-5.625E-01
750	45	Mo	Kr	1.67	-1.425E-01	1.646E+01	-3.562E+01	2.204E+01	-2.369E+00	1.894E-01	3.303E+01	-8.632E+01	8.539E+01	-3.954E+01	8.358E+00	-3.876E-01
750	60	Mo	Kr	1.51	-5.875E+00	3.748E+01	-7.017E+01	5.145E+01	-1.355E+01	1.249E+00	3.478E+01	-9.699E+01	1.035E+02	-5.186E+01	1.192E+01	-7.445E-01
1000	0	Mo	Kr	1.18	1.200E+01	-3.244E+01	3.381E+01	-1.821E+01	5.429E+00	-3.239E-01	-1.781E+01	5.880E+01	-7.054E+01	3.623E+01	-7.256E+00	8.500E-01
1000	15	Mo	Kr	1.29	1.638E+01	-4.104E+01	3.897E+01	-1.997E+01	6.450E+00	-3.740E-01	1.465E+01	-3.404E+01	3.015E+01	-1.434E+01	4.230E+00	-2.572E-01
1000	30	Mo	Kr	1.67	2.999E+01	-7.585E+01	7.169E+01	-3.484E+01	1.036E+01	-6.919E-01	4.414E+01	-1.158E+02	1.164E+02	-5.663E+01	1.336E+01	-8.594E-01
1000	45	Mo	Kr	1.87	-1.521E+00	2.321E+01	-4.605E+01	2.901E+01	-4.231E+00	2.994E-01	3.662E+01	-9.569E+01	9.495E+01	-4.437E+01	9.656E+00	-4.743E-01
1000	60	Mo	Kr	1.75	-1.501E+01	6.626E+01	-1.043E+02	7.060E+01	-1.847E+01	1.679E+00	3.714E+01	-1.047E+02	1.138E+02	-5.872E+01	1.411E+01	-9.108E-01
1500	0	Mo	Kr	1.19	8.132E+00	-1.967E+01	1.741E+01	-7.888E+00	2.443E+00	-7.334E-02	6.249E+00	-1.472E+01	1.231E+01	-5.652E+00	2.125E+00	2.700E-02
1500	15	Mo	Kr	1.47	7.688E+00	-1.762E+01	1.528E+01	-8.557E+00	3.928E+00	-1.879E-01	2.642E+01	-6.632E+01	6.163E+01	-2.707E+01	6.142E+00	-3.043E-01
1500	30	Mo	Kr	2.01	1.849E+01	-4.634E+01	4.538E+01	-2.538E+01	9.325E+00	-6.712E-01	4.998E+01	-1.325E+02	1.354E+02	-6.750E+01	1.651E+01	-1.100E+00
1500	45	Mo	Kr	2.21	-1.196E+01	5.294E+01	-7.703E+01	4.394E+01	-7.509E+00	5.412E-01	3.431E+01	-8.895E+01	8.862E+01	-4.250E+01	9.901E+00	-4.714E-01
1500	60	Mo	Kr	2.15	-1.062E+01	5.715E+01	-9.950E+01	7.205E+01	-2.000E+01	1.875E+00	2.535E+01	-6.818E+01	7.159E+01	-3.606E+01	8.397E+00	-1.349E-01

$$y(\alpha) = A_6 \cos^6(\alpha) + A_5 \cos^5(\alpha) + A_4 \cos^4(\alpha) + A_3 \cos^3(\alpha) + A_2 \cos^2(\alpha) + A_1 \cos(\alpha) \qquad 0^o \le \alpha < 90^o$$

$$y(\alpha) = B_6 \cos^6(\alpha) + B_5 \cos^5(\alpha) + B_4 \cos^4(\alpha) + B_3 \cos^3(\alpha) + B_2 \cos^2(\alpha) + B_1 \cos(\alpha) \qquad -90^o \le \alpha < 0^o$$

$$Y = \sum_{i=1}^{6} \frac{\pi}{i+1} A_i + \sum_{i=1}^{6} \frac{\pi}{i+1} B_i$$

E (eV)	β °	Target	Ion	Y (atoms/ion)	A6	A5	A4	A3	A2	A1	B6	B5	B4	B3	B2	B1
150	0	Ta	Xe	0.05	-4.795E-01	1.155E+00	-7.751E-01	-2.819E-02	1.097E-01	1.972E-02	-1.248E+00	3.871E+00	-4.396E+00	2.194E+00	-4.926E-01	7.343E-02
200	0	Ta	Xe	0.14	-1.035E+00	3.020E+00	-2.804E+00	7.250E-01	1.805E-02	8.056E-02	-1.008E+00	2.573E+00	-1.666E+00	-3.911E-01	4.797E-01	1.677E-02
300	0	Ta	Xe	0.36	-6.179E-01	1.504E+00	1.232E-01	-2.389E+00	1.445E+00	-3.391E-02	-4.145E+00	1.276E+01	-1.327E+01	4.833E+00	-2.668E-01	1.197E-01
300	15	Ta	Xe	0.47	-1.244E+01	3.578E+01	-3.491E+01	1.167E+01	-1.164E-01	6.812E-02	9.935E-01	-2.337E+00	3.156E+00	-3.003E+00	1.328E+00	-8.617E-02
300	30	Ta	Xe	0.63	-3.217E+01	9.859E+01	-1.101E+02	5.259E+01	-9.717E+00	9.245E-01	1.045E+01	-2.942E+01	3.193E+01	-1.662E+01	3.996E+00	-2.614E-01
300	45	Ta	Xe	0.66	-1.061E+01	3.260E+01	-3.537E+01	1.436E+01	-1.007E+00	1.796E-01	1.832E+01	-4.926E+01	4.944E+01	-2.273E+01	4.626E+00	-2.664E-01
300	60	Ta	Xe	0.48	-6.418E+00	1.944E+01	-2.110E+01	8.760E+00	-5.550E-01	4.311E-02	1.800E+01	-5.235E+01	5.785E+01	-2.967E+01	6.803E+00	-4.892E-01
400	0	Ta	Xe	0.57	-3.452E+00	1.140E+01	-1.211E+01	3.990E+00	1.083E-01	1.464E-01	-7.496E+00	2.361E+01	-2.565E+01	1.055E+01	-1.119E+00	1.826E-01
500	0	Ta	Xe	0.69	-3.298E+00	1.174E+01	-1.321E+01	4.694E+00	4.791E-02	1.504E-01	-4.149E+00	1.434E+01	-1.593E+01	5.663E+00	7.041E-02	1.209E-01
500	15	Ta	Xe	0.64	-1.069E+00	3.985E+00	-4.055E+00	-4.476E-01	1.796E+00	-8.990E-02	8.166E+00	-2.134E+01	2.152E+01	-1.089E+01	2.761E+00	-1.002E-01
500	30	Ta	Xe	0.79	-1.700E+01	4.986E+01	-5.276E+01	2.239E+01	-2.689E+00	3.531E-01	1.750E+01	-4.652E+01	4.626E+01	-2.111E+01	4.115E+00	-1.024E-01
500	45	Ta	Xe	0.86	-1.030E+01	3.441E+01	-4.131E+01	1.954E+01	-2.216E+00	1.493E-01	2.608E+01	-6.951E+01	6.907E+01	-3.131E+01	6.204E+00	-2.920E-01
500	60	Ta	Xe	0.67	-5.025E+00	1.633E+01	-1.881E+01	7.942E+00	-2.576E-02	-1.222E-01	2.024E+01	-5.718E+01	6.201E+01	-3.166E+01	7.361E+00	-4.918E-01
750	0	Ta	Xe	0.92	-7.306E+00	2.715E+01	-3.481E+01	1.824E+01	-3.514E+00	4.749E-01	-1.819E+00	1.049E+01	-1.565E+01	7.942E+00	-1.006E+00	2.742E-01
750	15	Ta	Xe	1.04	-7.239E+00	2.348E+01	-2.500E+01	8.053E+00	1.078E+00	-5.426E-02	1.134E+01	-2.761E+01	2.655E+01	-1.369E+01	3.923E+00	-2.157E-01
750	30	Ta	Xe	1.25	-2.749E+01	8.682E+01	-1.005E+02	4.986E+01	-9.096E+00	8.510E-01	3.140E+01	-8.690E+01	9.321E+01	-4.846E+01	1.192E+01	-8.064E-01
750	45	Ta	Xe	1.32	-3.034E+01	9.831E+01	-1.158E+02	5.751E+01	-9.718E+00	5.639E-01	4.381E+01	-1.158E+02	1.144E+02	-5.221E+01	1.082E+01	-5.938E-01
750	60	Ta	Xe	1.10	-2.520E-01	8.334E+00	-1.637E+01	8.294E+00	1.196E+00	-6.652E-01	3.444E+01	-9.647E+01	1.031E+02	-5.131E+01	1.132E+01	-5.512E-01
1000	0	Ta	Xe	1.11	-6.225E+00	2.342E+01	-2.940E+01	1.425E+01	-1.980E+00	2.731E-01	-9.523E+00	3.547E+01	-4.590E+01	2.477E+01	-5.136E+00	6.595E-01
1000	15	Ta	Xe	1.26	-6.751E+00	2.299E+01	-2.521E+01	8.353E+00	1.112E+00	-5.002E-02	1.389E+01	-3.436E+01	3.391E+01	-1.788E+01	5.140E+00	-2.827E-01
1000	30	Ta	Xe	1.54	-4.840E+01	1.496E+02	-1.699E+02	8.401E+01	-1.622E+01	1.405E+00	3.932E+01	-1.057E+02	1.089E+02	-5.377E+01	1.260E+01	-8.009E-01
1000	45	Ta	Xe	1.66	-2.836E+01	9.678E+01	-1.201E+02	6.320E+01	-1.151E+01	6.882E-01	3.748E+01	-9.657E+01	9.346E+01	-4.201E+01	8.617E+00	-3.210E-01
1000	60	Ta	Xe	1.44	-1.486E+01	4.934E+01	-6.185E+01	3.475E+01	-7.559E+00	7.846E-01	2.191E+01	-6.214E+01	6.941E+01	-3.753E+01	9.443E+00	-5.004E-01
1500	0	Ta	Xe	1.46	-9.641E+00	3.221E+01	-3.819E+01	1.860E+01	-2.893E+00	3.785E-01	-4.240E+00	1.828E+01	-2.506E+01	1.309E+01	-2.020E+00	4.237E-01
1500	15	Ta	Xe	1.66	-1.194E+01	3.642E+01	-3.700E+01	1.210E+01	1.119E+00	-5.459E-02	2.210E+01	-5.512E+01	5.281E+01	-2.540E+01	6.584E+00	-3.679E-01
1500	30	Ta	Xe	2.02	-3.585E+01	1.112E+02	-1.248E+02	5.897E+01	-9.466E+00	7.433E-01	4.596E+01	-1.242E+02	1.304E+02	-6.703E+01	1.682E+01	-1.152E+00
1500	45	Ta	Xe	2.18	-5.006E+01	1.554E+02	-1.761E+02	8.500E+01	-1.409E+01	7.141E-01	5.007E+01	-1.339E+02	1.367E+02	-6.604E+01	1.503E+01	-8.439E-01
1500	60	Ta	Xe	2.09	-1.624E+01	6.285E+01	-8.987E+01	5.747E+01	-1.473E+01	1.474E+00	4.051E+01	-1.231E+02	1.487E+02	-8.782E+01	2.463E+01	-1.939E+00

$$y(\alpha) = A_6 \cos^6(\alpha) + A_5 \cos^5(\alpha) + A_4 \cos^4(\alpha) + A_3 \cos^3(\alpha) + A_2 \cos^2(\alpha) + A_1 \cos(\alpha) \qquad 0^o \le \alpha < 90^o$$

$$y(\alpha) = B_6 \cos^6(\alpha) + B_5 \cos^5(\alpha) + B_4 \cos^4(\alpha) + B_3 \cos^3(\alpha) + B_2 \cos^2(\alpha) + B_1 \cos(\alpha) \qquad -90^o \le \alpha < 0^o$$

$$Y = \sum_{i=1}^{6} \frac{\pi}{i+1} A_i + \sum_{i=1}^{6} \frac{\pi}{i+1} B_i$$

E (eV)	β °	Target	Ion	Y (atoms/ion)	A6	A5	A4	A3	A2	A1	B6	B5	B4	B3	B2	B1
500	0	Ta	Ar	0.43	-2.486E+00	8.413E+00	-9.773E+00	4.411E+00	-5.711E-01	1.431E-01	5.502E+00	-1.479E+01	1.531E+01	-7.909E+00	2.132E+00	-1.095E-01
500	15	Ta	Ar	0.51	-4.244E+00	1.249E+01	-1.204E+01	3.396E+00	6.009E-01	-3.691E-02	4.629E+00	-1.136E+01	1.085E+01	-5.494E+00	1.587E+00	-5.633E-02
500	30	Ta	Ar	0.62	-9.069E+00	2.855E+01	-3.227E+01	1.515E+01	-2.506E+00	3.472E-01	6.840E+00	-1.733E+01	1.701E+01	-8.419E+00	2.193E+00	-1.003E-01
500	45	Ta	Ar	0.68	-8.581E+00	2.668E+01	-2.862E+01	1.127E+01	-5.775E-01	4.629E-02	7.966E+00	-2.092E+01	2.131E+01	-1.068E+01	2.606E+00	-8.003E-02
500	60	Ta	Ar	0.59	-2.146E+01	7.365E+01	-9.475E+01	5.527E+01	-1.380E+01	1.279E+00	3.209E+00	-8.472E+00	9.452E+00	-5.711E+00	1.714E+00	-1.593E-02
750	0	Ta	Ar	0.62	-4.904E+00	1.548E+01	-1.708E+01	7.482E+00	-9.272E-01	1.563E-01	2.488E+00	-4.868E+00	3.532E+00	-1.803E+00	8.088E-01	4.912E-02
750	15	Ta	Ar	0.71	-5.198E+00	1.568E+01	-1.527E+01	4.294E+00	8.042E-01	-4.671E-02	5.475E+00	-1.258E+01	1.133E+01	-5.753E+00	1.870E+00	-8.810E-02
750	30	Ta	Ar	0.85	-1.312E+01	4.164E+01	-4.700E+01	2.194E+01	-3.516E+00	3.753E-01	7.313E+00	-1.781E+01	1.760E+01	-9.505E+00	2.804E+00	-9.890E-02
750	45	Ta	Ar	0.86	-1.465E+01	4.616E+01	-5.133E+01	2.288E+01	-2.925E+00	1.819E-01	1.250E+01	-3.222E+01	3.191E+01	-1.548E+01	3.741E+00	-1.429E-01
750	60	Ta	Ar	0.82	-2.592E+01	9.021E+01	-1.173E+02	6.924E+01	-1.765E+01	1.687E+00	7.780E+00	-2.153E+01	2.401E+01	-1.353E+01	3.606E+00	-5.756E-02
1000	0	Ta	Ar	0.67	-3.100E+00	1.004E+01	-1.026E+01	3.135E+00	4.044E-01	2.930E-02	2.635E+00	-4.652E+00	2.989E+00	-1.725E+00	9.841E-01	1.304E-02
1000	15	Ta	Ar	0.81	-1.163E+01	3.569E+01	-3.806E+01	1.580E+01	-1.590E+00	1.084E-01	4.933E+00	-9.197E+00	5.814E+00	-2.237E+00	9.592E-01	2.669E-02
1000	30	Ta	Ar	0.99	-1.526E+01	4.828E+01	-5.407E+01	2.502E+01	-4.028E+00	4.532E-01	1.930E+01	-5.299E+01	5.715E+01	-3.066E+01	8.159E+00	-5.735E-01
1000	45	Ta	Ar	0.99	-1.420E+01	4.620E+01	-5.293E+01	2.449E+01	-3.366E+00	1.992E-01	1.464E+01	-3.807E+01	3.826E+01	-1.896E+01	4.680E+00	-1.721E-01
1000	60	Ta	Ar	0.95	-1.805E+01	6.338E+01	-8.291E+01	4.886E+01	-1.215E+01	1.191E+00	3.812E+00	-8.530E+00	8.340E+00	-5.219E+00	1.839E+00	7.534E-02
1500	0	Ta	Ar	0.82	-6.722E+00	2.055E+01	-2.135E+01	8.231E+00	-5.156E-01	1.025E-01	2.164E-01	2.687E+00	-5.057E+00	2.115E+00	2.066E-01	1.286E-01
1500	15	Ta	Ar	1.02	-3.922E+00	1.347E+01	-1.405E+01	3.927E+00	9.770E-01	2.100E-03	-5.265E+00	1.970E+01	-2.402E+01	1.140E+01	-1.670E+00	2.424E-01
1500	30	Ta	Ar	1.25	-6.954E+00	2.404E+01	-2.701E+01	1.059E+01	-2.134E-01	5.634E-02	1.176E+01	-2.958E+01	3.037E+01	-1.682E+01	4.949E+00	-1.734E-01
1500	45	Ta	Ar	1.22	-2.070E+01	6.809E+01	-8.037E+01	4.024E+01	-7.284E+00	5.177E-01	1.067E+01	-2.847E+01	3.132E+01	-1.825E+01	5.484E+00	-2.494E-01
1500	60	Ta	Ar	1.23	1.540E+01	-3.856E+01	3.374E+01	-1.237E+01	2.230E+00	1.813E-02	-6.315E+00	2.042E+01	-2.192E+01	8.953E+00	-1.202E+00	5.112E-01

$$y(\alpha) = A_6 \cos^6(\alpha) + A_5 \cos^5(\alpha) + A_4 \cos^4(\alpha) + A_3 \cos^3(\alpha) + A_2 \cos^2(\alpha) + A_1 \cos(\alpha) \qquad 0^o \le \alpha < 90^o$$

$$y(\alpha) = B_6 \cos^6(\alpha) + B_5 \cos^5(\alpha) + B_4 \cos^4(\alpha) + B_3 \cos^3(\alpha) + B_2 \cos^2(\alpha) + B_1 \cos(\alpha) \qquad -90^o \le \alpha < 0^o$$

$$Y = \sum_{i=1}^{6} \frac{\pi}{i+1} A_i + \sum_{i=1}^{6} \frac{\pi}{i+1} B_i$$

E (eV)	β °	Target	Ion	Y (atoms/ion)	A6	A5	A4	A3	A2	A1	B6	B5	B4	B3	B2	B1
500	0	Ta	Kr	0.58	-2.199E+00	1.072E+01	-1.651E+01	1.021E+01	-2.435E+00	3.620E-01	5.969E+00	-1.673E+01	1.839E+01	-1.030E+01	2.892E+00	-7.766E-02
500	15	Ta	Kr	0.67	-6.870E+00	1.978E+01	-1.919E+01	5.746E+00	7.392E-01	-4.325E-02	4.224E+00	-9.386E+00	8.013E+00	-3.918E+00	1.204E+00	2.096E-02
500	30	Ta	Kr	0.75	-2.017E+01	6.103E+01	-6.786E+01	3.247E+01	-5.921E+00	6.318E-01	1.638E+01	-4.627E+01	4.997E+01	-2.571E+01	6.224E+00	-4.202E-01
500	45	Ta	Kr	0.84	-1.181E+01	3.641E+01	-3.945E+01	1.594E+01	-8.571E-01	1.950E-02	1.732E+01	-4.559E+01	4.487E+01	-2.046E+01	4.277E+00	-1.810E-01
500	60	Ta	Kr	0.67	1.252E+00	3.307E+00	-1.474E+01	1.496E+01	-5.350E+00	8.135E-01	1.787E+01	-5.083E+01	5.521E+01	-2.818E+01	6.528E+00	-3.689E-01
750	0	Ta	Kr	0.88	-1.243E+01	3.757E+01	-4.016E+01	1.739E+01	-2.452E+00	3.329E-01	5.922E+00	-1.502E+01	1.519E+01	-8.560E+00	2.811E+00	-9.259E-02
750	15	Ta	Kr	1.02	-1.085E+01	3.337E+01	-3.514E+01	1.335E+01	-4.882E-01	9.153E-02	1.027E+01	-2.518E+01	2.428E+01	-1.245E+01	3.520E+00	-1.331E-01
750	30	Ta	Kr	1.15	-2.399E+01	7.266E+01	-7.943E+01	3.611E+01	-5.412E+00	4.580E-01	1.850E+01	-4.858E+01	4.962E+01	-2.519E+01	6.375E+00	-3.578E-01
750	45	Ta	Kr	1.19	-3.055E+01	9.653E+01	-1.111E+02	5.444E+01	-9.468E+00	6.032E-01	2.512E+01	-6.505E+01	6.338E+01	-2.896E+01	6.175E+00	-2.365E-01
750	60	Ta	Kr	1.14	-9.523E+00	3.525E+01	-4.797E+01	2.833E+01	-6.188E+00	5.640E-01	2.632E+01	-7.648E+01	8.630E+01	-4.665E+01	1.161E+01	-6.799E-01
1000	0	Ta	Kr	1.06	-1.385E+01	4.247E+01	-4.606E+01	2.029E+01	-2.886E+00	3.554E-01	8.326E-01	1.392E+00	-3.715E+00	9.972E-01	6.193E-01	1.958E-01
1000	15	Ta	Kr	1.20	-1.088E+01	3.320E+01	-3.345E+01	1.068E+01	9.584E-01	-8.464E-02	1.519E+01	-3.769E+01	3.617E+01	-1.782E+01	4.801E+00	-2.469E-01
1000	30	Ta	Kr	1.42	-2.296E+01	7.129E+01	-7.972E+01	3.728E+01	-5.854E+00	5.217E-01	4.001E+01	-1.090E+02	1.144E+02	-5.815E+01	1.420E+01	-9.194E-01
1000	45	Ta	Kr	1.42	-2.659E+01	8.736E+01	-1.033E+02	5.127E+01	-8.618E+00	4.640E-01	2.216E+01	-5.702E+01	5.636E+01	-2.700E+01	6.253E+00	-1.922E-01
1000	60	Ta	Kr	1.44	-7.771E+00	3.172E+01	-4.698E+01	3.041E+01	-7.599E+00	8.019E-01	2.816E+01	-7.587E+01	7.771E+01	-3.751E+01	8.233E+00	-1.604E-01
1500	0	Ta	Kr	1.33	-1.079E+01	3.309E+01	-3.464E+01	1.349E+01	-9.095E-01	2.158E-01	8.961E+00	-2.147E+01	2.114E+01	-1.219E+01	4.120E+00	-1.050E-01
1500	15	Ta	Kr	1.55	-2.102E+01	6.111E+01	-6.075E+01	2.189E+01	-6.323E-01	2.320E-02	1.901E+01	-4.660E+01	4.409E+01	-2.139E+01	5.781E+00	-3.114E-01
1500	30	Ta	Kr	1.84	-3.013E+01	9.340E+01	-1.039E+02	4.835E+01	-7.597E+00	6.099E-01	3.239E+01	-8.782E+01	9.406E+01	-5.041E+01	1.334E+01	-8.165E-01
1500	45	Ta	Kr	1.82	-3.642E+01	1.179E+02	-1.386E+02	6.989E+01	-1.278E+01	7.996E-01	2.478E+01	-6.490E+01	6.633E+01	-3.357E+01	8.451E+00	-3.398E-01
1500	60	Ta	Kr	1.79	-4.370E+00	2.257E+01	-3.807E+01	2.674E+01	-6.886E+00	7.466E-01	1.043E+01	-2.374E+01	2.200E+01	-1.150E+01	3.214E+00	3.077E-01

$$y(\alpha) = A_6 \cos^6(\alpha) + A_5 \cos^5(\alpha) + A_4 \cos^4(\alpha) + A_3 \cos^3(\alpha) + A_2 \cos^2(\alpha) + A_1 \cos(\alpha) \qquad 0^o \le \alpha < 90^o$$

$$y(\alpha) = B_6 \cos^6(\alpha) + B_5 \cos^5(\alpha) + B_4 \cos^4(\alpha) + B_3 \cos^3(\alpha) + B_2 \cos^2(\alpha) + B_1 \cos(\alpha) \qquad -90^o \le \alpha < 0^o$$

$$Y = \sum_{i=1}^{6} \frac{\pi}{i+1} A_i + \sum_{i=1}^{6} \frac{\pi}{i+1} B_i$$

E (eV)	β °	Target	Ion	Y (atoms/ion)	A6	A5	A4	A3	A2	A1	B6	B5	B4	B3	B2	B1
500	0	W	Xe	0.74	5.166E+00	-1.432E+01	1.572E+01	-9.500E+00	3.196E+00	-1.579E-01	1.675E+00	-3.437E+00	2.703E+00	-2.133E+00	1.158E+00	1.393E-01
500	5	W	Xe	0.74	9.299E+00	-2.738E+01	3.175E+01	-1.916E+01	6.013E+00	-3.908E-01	1.224E+01	-3.425E+01	3.706E+01	-2.022E+01	5.667E+00	-3.676E-01
500	15	W	Xe	0.83	1.119E+00	-1.411E+00	4.254E-01	-2.337E+00	2.531E+00	-1.881E-01	9.066E+00	-2.497E+01	2.674E+01	-1.441E+01	3.852E+00	-1.506E-01
500	30	W	Xe	0.92	-4.156E+00	1.677E+01	-2.427E+01	1.317E+01	-1.533E+00	2.143E-01	1.772E+01	-4.764E+01	4.863E+01	-2.363E+01	5.393E+00	-3.096E-01
500	45	W	Xe	0.96	2.952E+00	-3.428E+00	-5.053E+00	6.730E+00	-1.087E+00	1.718E-01	2.654E+01	-7.053E+01	6.973E+01	-3.137E+01	6.149E+00	-2.622E-01
500	60	W	Xe	0.68	-1.436E+01	4.861E+01	-6.492E+01	4.055E+01	-1.048E+01	8.962E-01	1.955E+01	-5.594E+01	6.125E+01	-3.132E+01	7.198E+00	-4.607E-01
750	0	W	Xe	1.13	9.689E+00	-2.579E+01	2.666E+01	-1.469E+01	4.629E+00	-2.411E-01	-1.666E+00	1.020E+01	-1.632E+01	8.735E+00	-9.194E-01	2.355E-01
750	5	W	Xe	1.14	9.197E+00	-2.533E+01	2.757E+01	-1.638E+01	5.572E+00	-3.553E-01	1.222E+01	-3.249E+01	3.365E+01	-1.834E+01	5.504E+00	-2.776E-01
750	15	W	Xe	1.22	7.732E+00	-1.823E+01	1.609E+01	-9.066E+00	4.073E+00	-2.647E-01	1.424E+01	-3.679E+01	3.693E+01	-1.903E+01	5.207E+00	-2.419E-01
750	30	W	Xe	1.41	7.304E+00	-1.517E+01	8.958E+00	-3.132E+00	2.534E+00	-7.463E-02	2.853E+01	-7.645E+01	7.828E+01	-3.845E+01	9.038E+00	-5.436E-01
750	45	W	Xe	1.49	1.778E-01	1.140E+01	-2.980E+01	2.360E+01	-5.391E+00	5.500E-01	3.255E+01	-8.608E+01	8.579E+01	-3.973E+01	8.335E+00	-3.593E-01
750	60	W	Xe	1.22	1.443E+01	-3.755E+01	3.066E+01	-7.277E+00	6.912E-02	1.939E-01	-7.309E+00	2.657E+01	-3.279E+01	1.754E+01	-4.095E+00	6.085E-01
1000	0	W	Xe	1.40	3.930E+00	-7.607E+00	5.086E+00	-2.861E+00	1.743E+00	7.174E-02	5.305E+00	-1.267E+01	1.229E+01	-8.022E+00	3.583E+00	-1.222E-01
1000	5	W	Xe	1.38	1.158E+01	-3.064E+01	3.151E+01	-1.750E+01	5.812E+00	-3.776E-01	1.078E+01	-2.819E+01	2.934E+01	-1.679E+01	5.515E+00	-2.704E-01
1000	15	W	Xe	1.45	1.193E+01	-2.910E+01	2.660E+01	-1.381E+01	5.179E+00	-3.390E-01	1.934E+01	-5.079E+01	5.134E+01	-2.597E+01	6.899E+00	-3.822E-01
1000	30	W	Xe	1.62	1.020E+01	-2.456E+01	2.049E+01	-9.303E+00	3.956E+00	-2.100E-01	2.640E+01	-6.871E+01	6.862E+01	-3.332E+01	7.939E+00	-3.858E-01
1000	45	W	Xe	1.71	2.551E+00	1.764E+00	-1.446E+01	1.222E+01	-1.483E+00	7.055E-02	2.734E+01	-7.204E+01	7.271E+01	-3.498E+01	7.984E+00	-3.510E-01
1000	60	W	Xe	1.52	3.833E+01	-1.142E+02	1.246E+02	-6.130E+01	1.445E+01	-1.151E+00	5.747E+00	-1.193E+01	9.686E+00	-3.967E+00	7.739E-01	3.573E-01
1500	0	W	Xe	1.77	1.311E+01	-3.591E+01	3.820E+01	-2.116E+01	6.708E+00	-4.399E-01	-9.462E+00	3.268E+01	-4.057E+01	2.086E+01	-3.658E+00	6.671E-01
1500	5	W	Xe	1.79	1.114E+01	-3.058E+01	3.360E+01	-2.017E+01	7.035E+00	-4.676E-01	1.929E+01	-5.305E+01	5.655E+01	-3.066E+01	8.873E+00	-4.601E-01
1500	15	W	Xe	1.86	7.790E+00	-1.737E+01	1.499E+01	-9.053E+00	4.600E+00	-3.052E-01	1.984E+01	-5.043E+01	4.945E+01	-2.494E+01	7.008E+00	-3.198E-01
1500	30	W	Xe	2.06	3.456E+01	-9.589E+01	9.998E+01	-5.090E+01	1.416E+01	-1.106E+00	2.314E+01	-5.647E+01	5.314E+01	-2.518E+01	6.316E+00	-1.443E-01
1500	45	W	Xe	2.13	1.559E+00	7.245E+00	-2.287E+01	1.751E+01	-2.712E+00	1.510E-01	1.893E+01	-4.962E+01	5.150E+01	-2.659E+01	6.859E+00	-2.061E-01
1500	60	W	Xe	2.04	6.286E+01	-1.859E+02	2.015E+02	-9.695E+01	2.069E+01	-1.269E+00	-2.773E+01	8.808E+01	-1.023E+02	5.370E+01	-1.251E+01	1.636E+00

$$y(\alpha) = A_6 \cos^6(\alpha) + A_5 \cos^5(\alpha) + A_4 \cos^4(\alpha) + A_3 \cos^3(\alpha) + A_2 \cos^2(\alpha) + A_1 \cos(\alpha) \qquad 0^o \le \alpha < 90^o$$

$$y(\alpha) = B_6 \cos^6(\alpha) + B_5 \cos^5(\alpha) + B_4 \cos^4(\alpha) + B_3 \cos^3(\alpha) + B_2 \cos^2(\alpha) + B_1 \cos(\alpha) \qquad -90^o \le \alpha < 0^o$$

$$Y = \sum_{i=1}^{6} \frac{\pi}{i+1} A_i + \sum_{i=1}^{6} \frac{\pi}{i+1} B_i$$

E (eV)	β °	Target	Ion	Y (atoms/ion)	A6	A5	A4	A3	A2	A1	B6	B5	B4	B3	B2	B1
500	0	W	Ar	0.51	5.610E+00	-1.618E+01	1.806E+01	-1.004E+01	2.895E+00	-1.911E-01	-5.513E-01	3.373E+00	-5.300E+00	2.810E+00	-3.143E-01	1.346E-01
500	5	W	Ar	0.52	4.108E+00	-1.113E+01	1.192E+01	-6.797E+00	2.200E+00	-1.234E-01	8.253E+00	-2.205E+01	2.230E+01	-1.107E+01	2.900E+00	-1.699E-01
500	15	W	Ar	0.54	4.629E+00	-1.136E+01	1.041E+01	-5.117E+00	1.718E+00	-1.037E-01	5.847E+00	-1.475E+01	1.407E+01	-6.687E+00	1.694E+00	-2.750E-03
500	30	W	Ar	0.60	1.007E+01	-2.775E+01	2.883E+01	-1.479E+01	4.100E+00	-2.699E-01	1.329E+00	-1.196E+00	-8.694E-01	8.432E-01	-1.422E-02	1.051E-01
500	45	W	Ar	0.65	-4.319E+00	1.814E+01	-2.712E+01	1.719E+01	-4.149E+00	4.645E-01	1.686E+00	-4.029E+00	4.484E+00	-2.998E+00	1.001E+00	6.040E-02
500	60	W	Ar	0.57	-7.395E+00	3.138E+01	-4.864E+01	3.324E+01	-9.245E+00	8.586E-01	1.416E+00	-1.952E+00	-1.005E-01	1.122E+00	-5.374E-01	2.405E-01
750	0	W	Ar	0.70	2.926E+00	-7.436E+00	7.541E+00	-4.409E+00	1.670E+00	-7.588E-02	-6.079E-01	3.823E+00	-5.911E+00	2.973E+00	-2.163E-01	1.619E-01
750	5	W	Ar	0.67	5.712E+00	-1.530E+01	1.604E+01	-8.771E+00	2.698E+00	-1.488E-01	6.296E+00	-1.630E+01	1.627E+01	-8.402E+00	2.442E+00	-8.818E-02
750	15	W	Ar	0.72	8.749E+00	-2.177E+01	2.034E+01	-9.720E+00	2.829E+00	-1.675E-01	8.480E+00	-2.089E+01	1.957E+01	-9.320E+00	2.493E+00	-7.092E-02
750	30	W	Ar	0.80	2.372E+01	-6.545E+01	6.794E+01	-3.372E+01	8.475E+00	-6.351E-01	3.468E+00	-5.380E+00	2.090E+00	-2.696E-01	2.828E-01	1.362E-01
750	45	W	Ar	0.85	7.915E-01	3.662E+00	-1.139E+01	8.926E+00	-1.886E+00	2.085E-01	-3.009E+00	9.417E+00	-9.185E+00	2.857E+00	9.905E-02	1.379E-01
750	60	W	Ar	0.83	9.257E-01	9.080E+00	-2.684E+01	2.381E+01	-7.396E+00	7.280E-01	-8.126E+00	2.685E+01	-3.206E+01	1.694E+01	-3.866E+00	5.680E-01
1000	0	W	Ar	0.75	6.670E+00	-1.834E+01	1.959E+01	-1.069E+01	3.223E+00	-2.081E-01	3.288E+00	-1.300E+01	2.141E+01	-1.787E+01	7.213E+00	-7.969E-01
1000	15	W	Ar	0.85	1.160E+01	-2.922E+01	2.796E+01	-1.368E+01	3.911E+00	-2.400E-01	1.182E+01	-2.974E+01	2.836E+01	-1.347E+01	3.490E+00	-1.425E-01
1000	30	W	Ar	0.98	3.618E+01	-1.006E+02	1.054E+02	-5.261E+01	1.306E+01	-1.047E+00	5.463E+00	-9.185E+00	4.438E+00	-9.106E-01	4.158E-01	2.052E-01
1000	45	W	Ar	1.01	1.041E+01	-2.465E+01	2.022E+01	-7.652E+00	2.211E+00	-1.584E-01	-1.538E+01	4.426E+01	-4.469E+01	1.856E+01	-2.648E+00	3.085E-01
1000	60	W	Ar	1.04	1.243E+01	-2.532E+01	1.232E+01	3.176E+00	-2.573E+00	3.640E-01	-2.372E+01	7.279E+01	-8.180E+01	4.107E+01	-9.015E+00	1.098E+00
1500	0	W	Ar	0.92	7.257E+00	-1.916E+01	1.995E+01	-1.095E+01	3.406E+00	-1.861E-01	3.077E+00	-7.355E+00	7.454E+00	-4.763E+00	1.891E+00	2.058E-02
1500	15	W	Ar	1.01	1.065E+01	-2.593E+01	2.413E+01	-1.189E+01	3.674E+00	-2.252E-01	1.682E+01	-4.395E+01	4.341E+01	-2.071E+01	5.007E+00	-1.918E-01
1500	30	W	Ar	1.20	4.081E+01	-1.135E+02	1.195E+02	-6.005E+01	1.498E+01	-1.194E+00	2.200E+00	3.884E-01	-5.822E+00	3.741E+00	-2.654E-01	2.650E-01
1500	45	W	Ar	1.30	1.729E+01	-4.601E+01	4.603E+01	-2.279E+01	6.612E+00	-6.843E-01	-3.234E+01	9.222E+01	-9.553E+01	4.268E+01	-7.233E+00	6.757E-01
1500	60	W	Ar	1.25	3.781E+01	-1.058E+02	1.089E+02	-5.022E+01	1.047E+01	-6.708E-01	-3.378E+01	1.044E+02	-1.193E+02	6.156E+01	-1.413E+01	1.716E+00

$$y(\alpha) = A_6 \cos^6(\alpha) + A_5 \cos^5(\alpha) + A_4 \cos^4(\alpha) + A_3 \cos^3(\alpha) + A_2 \cos^2(\alpha) + A_1 \cos(\alpha) \qquad 0^o \le \alpha < 90^o$$

$$y(\alpha) = B_6 \cos^6(\alpha) + B_5 \cos^5(\alpha) + B_4 \cos^4(\alpha) + B_3 \cos^3(\alpha) + B_2 \cos^2(\alpha) + B_1 \cos(\alpha) \qquad -90^o \le \alpha < 0^o$$

$$Y = \sum_{i=1}^{6} \frac{\pi}{i+1} A_i + \sum_{i=1}^{6} \frac{\pi}{i+1} B_i$$

E (eV)	β °	Target	Ion	Y (atoms/ion)	A6	A5	A4	A3	A2	A1	B6	B5	B4	B3	B2	B1
500	0	W	Kr	0.72	1.056E+01	-3.099E+01	3.524E+01	-2.004E+01	5.819E+00	-4.405E-01	-6.362E+00	2.194E+01	-2.714E+01	1.407E+01	-2.767E+00	4.278E-01
500	15	W	Kr	0.79	-3.159E-01	2.103E+00	-2.451E+00	-8.650E-01	1.851E+00	-1.297E-01	5.687E+00	-1.488E+01	1.593E+01	-9.499E+00	3.100E+00	-1.554E-01
500	30	W	Kr	0.87	6.144E+00	-1.658E+01	1.757E+01	-1.110E+01	4.566E+00	-3.701E-01	8.001E+00	-2.011E+01	1.982E+01	-1.010E+01	2.712E+00	-9.504E-02
500	45	W	Kr	0.88	5.058E-01	7.677E+00	-2.138E+01	1.749E+01	-4.526E+00	5.062E-01	1.161E+01	-3.055E+01	3.097E+01	-1.513E+01	3.456E+00	-8.068E-02
500	60	W	Kr	0.75	1.658E+01	-4.599E+01	4.447E+01	-1.795E+01	3.259E+00	-1.009E-01	-1.239E-01	3.652E+00	-6.640E+00	4.245E+00	-1.210E+00	3.442E-01
750	0	W	Kr	1.05	-2.741E+00	7.167E+00	-5.538E+00	-1.635E-01	1.599E+00	-6.025E-02	-6.248E+00	2.184E+01	-2.680E+01	1.321E+01	-2.085E+00	3.641E-01
750	15	W	Kr	1.10	1.123E+01	-2.792E+01	2.630E+01	-1.353E+01	4.576E+00	-2.989E-01	1.365E+01	-3.528E+01	3.527E+01	-1.801E+01	4.952E+00	-2.517E-01
750	30	W	Kr	1.22	1.951E+01	-5.158E+01	5.070E+01	-2.483E+01	7.118E+00	-5.071E-01	1.447E+01	-3.729E+01	3.774E+01	-1.940E+01	5.139E+00	-2.373E-01
750	45	W	Kr	1.27	-2.222E+00	1.909E+01	-3.767E+01	2.725E+01	-6.627E+00	6.356E-01	9.748E+00	-2.466E+01	2.481E+01	-1.266E+01	3.205E+00	9.605E-03
750	60	W	Kr	1.14	2.988E+01	-8.223E+01	8.024E+01	-3.331E+01	6.186E+00	-3.020E-01	-2.205E+00	1.117E+01	-1.598E+01	9.094E+00	-2.139E+00	5.154E-01
1000	0	W	Kr	1.20	9.760E+00	-2.607E+01	2.748E+01	-1.567E+01	5.294E+00	-4.397E-01	-7.334E+00	2.602E+01	-3.227E+01	1.617E+01	-2.637E+00	4.180E-01
1000	15	W	Kr	1.29	1.275E+01	-3.049E+01	2.744E+01	-1.362E+01	4.690E+00	-3.093E-01	1.559E+01	-3.948E+01	3.866E+01	-1.955E+01	5.514E+00	-3.014E-01
1000	30	W	Kr	1.42	3.926E+01	-1.090E+02	1.138E+02	-5.711E+01	1.481E+01	-1.164E+00	2.281E+01	-5.850E+01	5.819E+01	-2.890E+01	7.313E+00	-3.576E-01
1000	45	W	Kr	1.46	3.063E+00	3.226E+00	-1.830E+01	1.522E+01	-2.825E+00	1.994E-01	1.226E+01	-3.213E+01	3.410E+01	-1.872E+01	5.289E+00	-2.269E-01
1000	60	W	Kr	1.37	3.219E+01	-8.483E+01	7.770E+01	-2.864E+01	4.245E+00	-8.981E-02	-3.560E+00	1.505E+01	-2.002E+01	1.102E+01	-2.592E+00	6.691E-01
1500	0	W	Kr	1.47	1.306E+01	-3.674E+01	4.050E+01	-2.294E+01	7.058E+00	-4.894E-01	-1.272E+01	4.058E+01	-4.652E+01	2.226E+01	-3.709E+00	5.636E-01
1500	15	W	Kr	1.56	1.796E+01	-4.437E+01	4.133E+01	-2.010E+01	6.185E+00	-4.103E-01	2.468E+01	-6.454E+01	6.476E+01	-3.230E+01	8.413E+00	-4.414E-01
1500	30	W	Kr	1.72	4.913E+01	-1.368E+02	1.438E+02	-7.260E+01	1.870E+01	-1.537E+00	4.242E+00	-3.399E+00	-2.321E+00	1.349E+00	5.955E-01	2.766E-01
1500	45	W	Kr	1.75	1.953E+00	7.211E+00	-2.412E+01	1.966E+01	-4.271E+00	2.859E-01	-8.861E+00	2.567E+01	-2.291E+01	5.625E+00	1.096E+00	1.307E-01
1500	60	W	Kr	1.57	-9.341E+01	2.802E+02	-3.150E+02	1.628E+02	-3.745E+01	3.582E+00	9.783E+01	-3.080E+02	3.632E+02	-1.953E+02	4.665E+01	-3.737E+00

$$y(\alpha) = A_6 \cos^6(\alpha) + A_5 \cos^5(\alpha) + A_4 \cos^4(\alpha) + A_3 \cos^3(\alpha) + A_2 \cos^2(\alpha) + A_1 \cos(\alpha) \qquad 0^o \le \alpha < 90^o$$

$$y(\alpha) = B_6 \cos^6(\alpha) + B_5 \cos^5(\alpha) + B_4 \cos^4(\alpha) + B_3 \cos^3(\alpha) + B_2 \cos^2(\alpha) + B_1 \cos(\alpha) \qquad -90^o \le \alpha < 0^o$$

$$Y = \sum_{i=1}^{6} \frac{\pi}{i+1} A_i + \sum_{i=1}^{6} \frac{\pi}{i+1} B_i$$

Acknowledgments

We would like to thank Rosa Muñoz of the McNair/PEAKS scholars program for performing many QCM measurements and Dr. David Burtner for supplying a tantalum target. Mark Buttweiler and Dustin Warner's help in maintaining the vacuum system used in these experiments is gratefully acknowledged. The financial support provided by the Jet Propulsion Laboratory and Air Force Research Labs, Edwards Air Force Base is also greatly appreciated.

References

[1]Duchemin, O., "An Investigation of Ion Engine Erosion by Low Energy Sputtering," Ph.D. Dissertation, California Institute of Technology, Pasadena, CA, 2001.

[2]Küstner, M., Eckstein, W., Dose, V., and Roth, J., "The Influence of Surface Roughness on the Angular Dependence of the Sputter Yield," *Nuclear Instruments and Methods in Physics Research B*, Vol. 145, 1998, p. 323.

[3]Küstner, M., Eckstein, W., Hechtl, E., and Roth, J., "Angular Dependence of the Sputtering Yield of Rough Beryllium Surfaces," *Journal of Nuclear Materials*, Vol. 265, No.1, 1999, pp. 22-27.

[4]Williams, J., Johnson, M., and Williams, D., "Differential Sputtering Behavior of Pyrolytic Graphite and Carbon-Carbon Composite Under Xenon Bombardment," *40th Joint Propulsion Conference,* AIAA Paper 2004-3788, 2004.

[5]Williams, J., Gardner, M., Johnson, M., and Wilbur, P., "Xenon Sputter Yield Measurements for Ion Thruster Materials," NASA CR-2003-212306, 2003.

[6]Mantenieks, M., Foster, J., Ray, P., Shutthanandan, S., and Thevuthasan, T., "Low Energy Xenon Ion Sputtering Yield Measurements," *27th International Electric Propulsion Conference*, IEPC-01-309, Pasadena, CA, 2001.

[7]Shutthanandan, V., Ray, P., Shivaparan, N., Smith, R., Thevuthasan, T., and Mantenieks, M., "On the Measurement of Low-Energy Sputtering Yield Using Rutherford Backscattering Spectrometry," *25th International Electric Propulsion Conference*, IEPC-97-069, Cleveland, OH, 1997.

[8]Nakles, M., "Experimental Modeling Studies of Low-Energy Ion Sputtering for Ion Thrusters," M.S. Thesis, Departmet of Aerospace Engineering, Virginia Polytechnic Institute, Blacksburg, VA, 2004.

[9]Oyarzabel, E., Yu, J., Hanna, J., Tynan, G., Doerner, R., Taylor, K., and Schmid, K., "Molybdenum and Carbon Cluster Angular Sputtering Distributions Under Low Energy Xenon Ion Bombardment," *41st Joint Propulsion Conference*, AIAA Paper 2005-3525, 2005.

[10]Wehner, G., and Rosenberg, D., "Angular Distribution of Sputtered Material," *Journal of Applied Physics*, Vol. 31, No. 1, 1960, pp. 177-179.

[11]Ziegler, J., Biersack, J., and Littmark, U., *The Stopping and Range of Ions in Solids*, Pergamon, New York, 1985.

[12]Abrams, C. and Graves, D., "Three-Dimensional Spatiokinetic Distributions of Sputtered and Scattered Products of Ar^+ and Cu^+ Impacts onto the Cu Surface: Molecular Dynamics Simulations," *IEEE Transactions on Plasma Science*, Vol. 27, No. 5, 1999, pp. 1426-1432.

[13]Doughty, C., Gorbatkin, S., and Berry, L., "Spatial Distribution of Cu Sputter Ejected by Very Low Energy Ion Bombardment," *Journal of Applied Physics*, Vol. 82, No. 4, 1997, pp. 1868-1875.

[14]Zhenxia, W., Wenyun, L., Chuanshan, W., and Wenmin, W., "Modelling of the Angular Distribution of Sputtered Particles from Roughened Elemental and Alloy Targets," *Vacuum*, Vol. 47, No. 12, 1996, pp. 1465-1472.

[15]Chini, T., Tanemura, M., and Okuyama, F., "Angular Distribution of Sputtered Ge Atoms by Low keV Ar^+ and Ne^+ Ion Bombardment," *Nuclear Instruments and Methods in Physics Research B*, Vol. 119, 1996, pp. 387-391.

[16]Betz, G., and Wien, K., "Energy and Angular Distributions of Sputtered Particles," *International Journal of Mass Spectrometry and Ion Precesses*, Vol. 140, 1994, pp. 1-110.

[17]Stein, R., and Hurlbut, F., "Angular Distribution of Sputtered Potassium Atoms," *Physical Review*, Vol. 123, No. 3, 1961, pp. 790-796.

[18]Huang, W., "Angular Resolved Sputtering Yields of Noble Metals and an Au-Ag Alloy," *Surface and Interface Analysis*, Vol. 14, 1989, pp. 469-476.

[19]Crofton, M., Murray, J., and Pollard, J., "Angular Properties of Xe^+-Sputtered Molybdenum at Low Impingement Energy," *Proceedings of the 4th International Spacecraft Propulsion Conference*, ESA SP-555.

[20]Whitaker, T., Li, A., Jones, P., and Watts, R., "Angular Distributions of Sputtered Zirconium Atoms," *Journal of Chemical Physics*, Vol. 98, No. 7, 1993, pp. 5887-5898.

[21]Surla, V., Wilbur, P., Johnson, M., Williams, J., and Yalin, A., "Sputter Erosion Measurements of Titanium and Molybdenum by Cavity Ring-Down Spectroscopy," *Review of Scientific Instruments*, Vol. 75, No. 9, 2004, pp. 3025-3030.

[22]Yalin, A., Surla, V., Buttweiler, M., and Williams, J., "Detection of Sputtered Metals using Cavity Ring-Down Spectroscopy," *Applied Optics*, expected: Vol. 44, No. 30, 2005.

[23]Kolasinski, R., "Oblique Angle Sputtering Yield Measurements for Ion Thruster Grid Materials," *41st Joint Propulsion Conference*, AIAA paper 2005-3526, 2005.

[24]Tartz, M., Neumann, H., Fritsche, B., Leiter, H., and Esch, J., "Investigation of Sputter Behaviour of Ion Thruster Grid Materials," *40th Joint Propulsion Conference,* AIAA Paper 2004-4114, 2004.

[25]Stepanova, M., and Dew, S., "Discrete-Path Transport Theory of Physical Sputtering," *Journal of Applied Physics*, Vol. 92, No. 3, 2002, pp.1699-1708.
[26]Stepanova, M., Dew, S., and Soshnikov, I., "Sputtering from Ion-Beam-Roughened Cu Surfaces," *Physical Review B*, Vol. 66, Sept. 2002, article #125407.
[27]Wåhlin, E., Watanabe, M., Shimonek, J., Burtner, D., and Siegfried, D., "Enhancement of Collimated Low-Energy Broad Beam Ion Source with Four-Grid Accelerator System," *Applied Physics Letters*, Vol. 83, No. 23, 2003, pp. 4722-4724.
[28]Zalm, P., "Quantitative Sputtering," *Surface and Interface Analysis*, Vol. 11, No. 1, 1988, pp. 1-24.
[29]Fine, J., "Absolute Sputtering Yield Measurement Methods: A Review", *Proceedings of the 10th Summer School and Symposium on Physics of Ionized Gases (SPIG 80)*, Dubrovnik, Yugoslavia, August 25-30, 1980.
[30]Yamamura, Y., Tawara, H., "Energy Dependence of Ion-Induced Sputtering Yields from Monatomic Solids at Normal Incidence," *Atomic Data and Nuclear Tables*, Vol. 62, No. 2, 1996, pp. 149-253.
[31]Doerner, R., Whyte, D., and Goebel, D., "Sputtering Yield Measurements During Low Energy Xenon Plasma Bombardment," *Journal of Applied Physics*, Vol. 93, No. 9, 2003, pp. 5816-5823.
[32]Doerner, R., and Goebel, D., "Sputtering Yields of Ion Thruster Grid and Cathode Materials During Very Low Xenon Plasma Bombardment," *39th Joint Propulsion Conference*, AIAA Paper 2003-4561, 2003.
[33]Blandino, J., Goodwin, G., and Garner, C., "Low Energy Sputter Yields for Diamond, Carbon-Carbon, Composite, and Molybdenum Subject to Xenon Ion Bombardment," *Diamond and Related Materials*, Vol. 9, No. 12, 2000, pp 1992-2001.